Inter-comparison and improvement of two-stream shortwave radiative transfer models in ESMs for a unified treatment of cryospheric surfaces

Cheng Dang[1], Charles S. Zender[1], Mark G. Flanner[2]

[1] Department of Earth System Science, University of California, Irvine, CA, USA

[2] Department of Climate and Space Sciences and Engineering, University of Michigan, Ann Arbor, MI, USA

Correspondence to: Cheng Dang (cdang5@uci.edu)

Abstract. Snow is an important climate regulator because it greatly increases the surface albedo of middle and high latitudes of the Earth. Earth System Models (ESMs) often adopt two-stream approximations with different radiative transfer techniques, the same snow therefore has different solar radiative properties depending whether it is on land or on sea ice. Here we inter-compare three two-stream algorithms widely used in snow models, improve their predictions at large zenith angles, and introduce a hybrid model suitable for all cryospheric surfaces in ESMs. The algorithms are those employed by the SNow ICe and Aerosol Radiative (SNICAR) module used in land models, and by dEdd-AD used in Icepack, the column physics used in the Los Alamos sea ice model CICE and MPAS-seaice, and a two-stream discrete ordinate (2SD) model. Compared with a 16-stream benchmark model, the errors in snow visible albedo for a direct-incident beam from all three two-stream models are small (<±0.005) and increase as snow shallows, especially for aged snow. The errors in direct near-infrared (near-IR) albedo are small (<±0.005) for solar zenith angles $\theta < 75°$, and increase as θ increases. For diffuse incidence under cloudy skies, dEdd-AD produces the most accurate snow albedo for both visible and near-IR (<±0.0002) with the lowest underestimate (-0.01) for melting thin snow. SNICAR performs similarly to dEdd-AD for visible albedos, with a slightly larger underestimate (-0.02), while it overestimates the near-IR albedo by an order of magnitude more (up to 0.04). 2SD overestimates both visible and near-IR albedo by up to 0.03. We develop a new parameterization that adjusts the underestimated direct near-IR albedo and overestimated direct near-IR heating persistent across all two-stream models for $\theta > 75°$. These results are incorporated in a hybrid model SNICAR-AD, which can now serve as a unified solar radiative transfer model for snow in ESM land, land ice, and sea-ice components.

1. Introduction

Snow cover on land, land ice, and sea ice, modulates the surface energy balance of middle and high latitudes of the Earth, principally because even a thin layer of snow can greatly increase the surface albedo. Integrated over the solar spectrum, the broadband albedo of opaque snow ranges from 0.7 – 0.9 (e.g., Wiscombe and Warren 1980; Dang et al., 2015). In contrast, the albedo of other natural surfaces is smaller: 0.2, 0.25, and 0.5-0.7 for damp soil, grassland, and bare multi-year sea ice, respectively (Perovich 1996; Liang et al., 2002; Brandt et al., 2005; Bøggild et al., 2010). The accumulation, evolution, and depletion of snow cover thus modify the seasonal cycle of surface albedo globally. In particular, snow over sea ice absorbs more solar energy and begins to melt in the spring, which forms melt ponds that bring the sea-ice albedo to as low as 0.15 to further accelerate ice melt (Light et al., 2008, 2015). An accurate simulation of the shortwave radiative properties of snowpack is therefore crucial for spectrally partitioning solar energy and representing snow-albedo feedbacks across the Earth system. Unfortunately, computational demands and coupling architectures often constrain representation of snowpack radiative processes in Earth System Models (ESMs, please refer to Table 1 for all acronyms used in this work) to relatively crude approximations such as two-stream methods (Wiscombe and Warren, 1980, Toon et al., 1989). In this work, we inter-compare two-stream methods widely used in snow models and then introduce a new parameterization that significantly reduces their snowpack reflectance and heating biases at large zenith angles, to produce more realistic behavior in polar regions.

Snow albedo is determined by many factors including the snow grain radius, the solar zenith angle, cloud transmittance, light-absorbing particles, and the albedo of underlying ground if snow is optically thin (Wiscombe and Warren, 1980; Warren and Wiscombe, 1980); it also varies strongly with wavelength since the ice absorption coefficient varies by 7 orders of magnitudes across the solar spectrum (Warren and Brandt, 2008). At visible wavelengths (0.2 - 0.7 μm), ice is almost non-absorptive such that the absorption of visible energy by snowpack is mostly due to the light-absorbing particles (e.g. black carbon, organic carbon, mineral dust) that were incorporated during ice nucleation in clouds, scavenged during precipitation, or slowly sedimented from the atmosphere by gravity (Warren and Wiscombe, 1980, 1985; Doherty et al., 2010, 2014, 2016; Wang et al., 2013; Dang and Hegg 2014). As snow becomes shallower, visible photons are more likely to penetrate through snowpack and get absorbed by darker underlying ground. At near-infrared (near-IR) wavelengths (0.7 – 5 μm), ice is much more absorptive, so that

72 the snow near-IR albedo is lower than the visible albedo. Larger ice crystals form a lower
73 albedo surface than smaller ice crystals hence aged snowpacks absorb more solar energy.
74 Photons incident at smaller solar zenith angles are more likely to penetrate deeper
75 vertically and be scattered in the snowpack until being absorbed by the ice/the underlying
76 ground/absorbing impurities, which also leads to a smaller snow albedo. To compute the
77 reflected solar flux, spectrally resolved albedo must be weighted by the incident solar
78 flux, which is mostly determined by solar zenith angle, cloud cover and transmittance,
79 and column water vapor. Modeling the solar properties of snowpacks must consider the
80 spectral signatures of these atmospheric properties.
81
82 Several parameterizations have been developed to compute the snow solar properties
83 without solving the radiative transfer equations and some are incorporated into ESMs or
84 regional models. Marshall and Warren (1987) and Marshall (1989) parameterized snow
85 albedo in both visible and near-IR bands as functions of snow grain size, solar zenith
86 angle, cloud transmittance, snow depth, underlying surface albedo, and black carbon
87 content. Marshall and Oglesby (1994) used this in an ESM. Gardner and Sharp (2010)
88 computed the all-wave snow albedo with similar inputs. This was incorporated into the
89 regional climate model RACMO
90 (https://www.projects.science.uu.nl/iceclimate/models/racmo.php) to simulate snow
91 albedo in glaciered regions like Antarctica and Greenland (Kuipers Munneke et al.,
92 2011). Dang et al., (2015) parameterized snow albedo as functions of snow grain radius,
93 black carbon content, and dust content for visible and near-IR bands and 14 narrower
94 bands used in the rapid radiative transfer model (RRTM, Mlawer and Clough, 1997).
95 Their algorithm can also be expanded to different solar zenith angles using the zenith
96 angle parameterization developed by Marshall and Warren (1987). Aoki et al., (2011)
97 developed a more complex model based on the offline snow albedo and a transmittance
98 look-up table. This can be applied to multilayer snowpack to compute the snow albedo
99 and the solar heating profiles as functions of snow grain size, black carbon and dust
100 content, snow temperature, and snowmelt water equivalent. These parameterizations are
101 often in the form of simplified polynomial equations, which are especially suitable to
102 long-term ESM simulations that require less time-consuming snow representations.
103
104 More complex models that explicitly solve the multiple scattering radiative transfer
105 equations have also been developed to compute snow solar properties. Flanner and
106 Zender (2005) developed the SNow Ice and Aerosol Radiation model (SNICAR) that
107 utilizes two-stream approximations (Wiscombe and Warren 1980; Toon et al., 1989) to

108 predict heating and reflectance for a multi-layer snowpack. They implemented SNICAR
109 in the Community Land Model (CLM) to predict snow albedo and vertically resolved
110 solar absorption for snow-covered surfaces. Before SNICAR, CLM prescribed snow
111 albedo and confined all solar absorption to the top snow layer (Flanner and Zender 2005).
112 Over the past decades, updates and new features have been added to SNICAR to consider
113 more processes such as black carbon/ice mixing states (Flanner et al., 2012) and snow
114 grain shape (He et al., 2018b). Concurrent with the development of SNICAR, Briegleb
115 and Light (2007) improved the treatment of sea-ice solar radiative calculations in
116 Community Climate System Model (CCSM). They implemented a different two-stream
117 scheme with delta-Eddington approximation and adding-doubling technique (hereafter,
118 dEdd-AD) that allows CCSM to compute bare/ponded/snow-covered sea ice albedo and
119 solar absorption profiles of multi-layer sea ice. Before these improvements, the sea-ice
120 albedo was computed based on surface temperature, snow thickness, and sea-ice
121 thickness using averaged sea ice and snow albedo. dEdd-AD has been adopted by the
122 sea-ice physics library Icepack (https://github.com/CICE-Consortium/Icepack/wiki),
123 which is used by the Los Almos Sea Ice Model CICE (Hunke et al., 2010) and Model for
124 Prediction Across Scales Sea Ice MPAS-seaice (Turner et al., 2018). CICE itself is used
125 in numerous global and regional models.
126
127 SNICAR and dEdd-AD solve the multiple scattering radiative transfer equations and
128 provide much improved solar radiative representations for the cryosphere, though their
129 separate development and implementation created an artificial divide for snow
130 simulation. In ESMs that utilize both SNICAR and dEdd-AD, such as the Community
131 Earth System Model (CESM, http://www.cesm.ucar.edu/) and the Energy Exscale Earth
132 System Model (E3SM, previously known as ACME, https://e3sm.org/), the solar
133 radiative properties of snow on land and snow on sea ice are computed separately via
134 SNICAR and dEdd-AD. As a result, the same snow in nature has different solar radiative
135 properties such as reflectance depending on which model represents it. These differences
136 are model artifacts that should be eliminated so that snow has consistent properties across
137 the Earth system.
138
139 In this paper, we evaluate the accuracy and biases of three two-stream models listed in
140 Table 2, including the algorithms used in SNICAR and dEdd-AD, for representing
141 reflectance and heating. In Sections 2-4, we describe the radiative transfer algorithms and
142 calculations performed in this work. The results and model inter-comparisons are
143 discussed in Section 5. In Section 6, we introduce a parameterization to reduce the

144 simulated albedo and heating bias for solar zenith angles larger than 75°. In Section 7, we
145 summarize the major differences of algorithm implementations between SNICAR and
146 dEdd-AD in ESMs. We use these results to develop and justify a unified surface
147 shortwave radiative transfer method for all Earth system model components in the
148 cryosphere, presented in Section 8.
149

150 **2. Radiative Transfer Model**
151
152 In this section, we summarize the three two-stream models and the benchmark DISORT
153 model with 16-streams. These algorithms are well documented in papers by Toon et al.,
154 (1989), Briegleb and Light (2007), Jin and Stamnes (1994), and Stamnes et al. (1988).
155 Readers interested in detailed mathematical derivations should refer to those papers. We
156 only include their key equations to illustrate the difference among two-stream models for
157 discussion purposes.

158
159 2.1 SNICAR in land models CLM and ELM
160 SNICAR is implemented as the default snow shortwave radiative transfer scheme in
161 CLM and E3SM land model (ELM). It adopts the two-stream algorithms and the rapid
162 solver developed by Toon et al., (1989) to compute the solar properties of multi-layer
163 snowpacks. These two-stream algorithms are derived from the general equation of
164 radiative transfer in a plane parallel media:

165

166 $\mu \frac{\partial I}{\partial \tau}(\tau, \mu, \Phi) = I(\tau, \mu, \Phi) - \frac{\varpi}{4\pi} \int_0^{2\pi} \int_{-1}^{1} P(\mu, \mu', \phi, \phi') I(\tau, \mu', \Phi') d\mu' d\phi' - S(\tau, \mu, \Phi)$

167
168   (1)
169
170
171 where Φ is azimuth angle, μ is the cosine of the zenith angle, ϖ is single-scattering
172 albedo. On the right-hand side, the three terms are intensity at optical depth τ, internal
173 source term due to multiple scattering, and external source term S. For a purely external
174 source at solar wavelengths S is:

175

176 $S = \frac{\varpi}{4} F_s P(\mu, -\mu_0, \phi, \phi_0) exp\left(\frac{-\tau}{\mu_0}\right)$ (2)

177

178 where πF_s is incident solar flux, μ_0 is the incident direction of the solar beam. Integrating
179 equation (1) over azimuth and zenith angles yields the general solution of two-stream

180   approximations (Meador and Weaver, 1980). The upward and downward fluxes at optical

181   depth τ of layer n can be represented as:

182

183

184    $$F_n^+ = k_{1n}\,exp(\Lambda_n\tau) + \Gamma_n k_{2n}\,exp(-\Lambda_n\tau) + C_n^+(\tau) \tag{3a}$$

185

186    $$F_n^- = \Gamma_n k_{1n}\,exp(\Lambda_n\tau) + k_{2n}\,exp(-\Lambda_n\tau) + C_n^-(\tau) \tag{3b}$$

187

188

189   where Λ_n, Γ_n C_n are known coefficients determined by the two-stream method, incident

190   solar flux, and solar zenith angle; whereas k_{1n} and k_{2n} are unknown coefficients

191   determined by the boundary conditions. For an N-layer snowpack, the solutions for

192   upward and downward fluxes are coupled at layer interfaces to generate 2N equations

193   with 2N unknown coefficients k_{1n} and k_{2n}. Combining these equations linearly generates

194   a new set of equations with terms in tridiagonal form that enables the application of a fast

195   tri-diagonal matrix solver. With the solved coefficients, the upward and downward fluxes

196   are computed at different optical depths (Equations 3a and 3b) and eventually the

197   reflectance, transmittance, and absorption profiles of solar flux for any multilayer

198   snowpack.

199

200   SNICAR itself implements all three two-stream algorithms in Toon et al., (1989):

201   Eddington, Quadrature, and Hemispheric-mean. In practical simulations, it utilizes the

202   Eddington and Hemispheric-mean approximations to compute the visible and near-IR

203   snow properties, respectively (Flanner et al., 2007). In addition to its algorithms,

204   SNICAR implements the Delta-transform of the fundamental input variables asymmetry

205   factor (g), single-scattering albedo (ϖ), and optical depth (τ) to account for the strong

206   forward scattering in snow (Equations 2 (a)-(c), Wiscombe and Warren, 1980).

207

208   2.2. dEdd-AD in sea ice models Icepack, CICE, and MPAS-seaice

209   Icepack, CICE, and MPAS-seaice use the same shortwave radiative scheme dEdd-AD

210   developed and documented by Briegleb and Light (2007). Sea ice is divided into multiple

211   layers to first compute the single-layer reflectance and transmittance using two-stream

212   delta-Eddington solutions to account for the multiple scattering of light within each layer

213   (Equation set 50, Briegleb and Light, 2007), where the name "delta" implies dEdd-AD

214   implements the Delta-transform to account for the strong forward scattering of snow and

215   sea ice (Equations 2 (a)-(c), Wiscombe and Warren, 1980). The single-layer direct albedo

216   and transmittance are computed by equations:

217

218    $$R(\mu_{0,n}) = A_n \, exp\left(\frac{-\tau}{\mu_{0,n}}\right) + B_n(exp(\varepsilon_n\tau) - exp(-\varepsilon_n\tau)) - K_n \qquad\qquad (4a)$$

219

220    $$T(\mu_{0,n}) = E_n + H_n(exp(\varepsilon_n\tau) - exp(-\varepsilon_n\tau)) \, exp\left(\frac{-\tau}{\mu_{0,n}}\right) \qquad\qquad (4b)$$

221

222   where coefficients A_n, B_n, K_n, E_n, H_n, and ε_n are determined by the single-scattering

223   albedo (ϖ), asymmetry factor (g), optical depth (τ), and angle of the incident beam at

224   layer n ($\mu_{0,n}$). Following the delta-Eddington assumption, simple formulas are available

225   for the single-layer reflectance and transmittance under both clear sky (direct flux,

226   equations 4a and 4b) and overcast sky (diffuse flux) conditions, however, the formula

227   derived by applying diffuse-flux upper boundary conditions sometimes yields negative

228   albedos (Wiscombe 1977). To avoid the unphysical values, diffuse reflectance $\bar{R}$ and

229   transmittance $\bar{T}$ of a single layer are computed by integrating the direct reflectance $R(\mu)$

230   and transmittance $T(\mu)$ over the incident hemisphere assuming isotropic incidence:

231

232    $$\bar{R} = 2\int_0^1 \mu R(\mu)d\mu \qquad\qquad (5a)$$

233

234    $$\bar{T} = 2\int_0^1 \mu T(\mu)d\mu \qquad\qquad (5b)$$

235

236   This is the same as the method proposed by Wiscombe and Warren (1980, their equation

237   5). In practice, eight Gaussian angles are implemented to perform the integration for

238   every layer.

239

240   The computed single-layer reflectance and transmittance of direct and diffuse

241   components are then combined to account for the inter-layer scattering of light to

242   compute the reflectance and transmission at every interface (Equation set 51, Briegleb

243   and Light, 2007), and eventually the upward and downward fluxes (Equation set 52,

244   Briegleb and Light, 2007). These upward and downward fluxes at each optical depth are

245   then used to compute the column reflectance and transmittance, and the absorption

246   profiles for any multilayered media, such as snowpacks on land and sea ice.

247

248   In nature, a large fraction of sea ice is covered by snow during winter. As snow melts

249   away in late spring and summer, it exposes bare ice, and melt ponds form on the ice

250 surface. Such variation of sea-ice surface types requires the shortwave radiative transfer
251 model to be flexible and capable of capturing the light refraction and reflection.
252 Refractive boundaries exist where air (refractive index $m_{re} = 1.0$), snow (assuming snow
253 as medium of air containing a collection of ice particles, $m_{re} = 1.0$), pond (assuming pure
254 water, $m_{re} = 1.33$), and ice (assuming pure ice, $m_{re} = 1.31$) are present in the same sea-ice
255 column. The general solution of delta-Eddington, and the two-stream algorithms used in
256 SNICAR are not applicable to such non-uniformly refractive layered media. To include
257 the effects of refraction, Briegleb and Light (2007) modified the adding formula at the
258 refractive boundaries (i.e. interfaces between air/ice, snow/ice, air/pond). The reflectance
259 and transmittance of the adjacent layers above and below the refractive boundary are
260 combined with modifications to include the Fresnel reflection and refraction of direct and
261 diffuse fluxes (Section 4.1, Briegleb and Light, 2007). dEdd-AD can thus be applied to
262 any layered media with either uniform (e.g., snow on land) or non-uniform (e.g., snow on
263 sea ice) refractive indexes.

264

265 In this paper, we apply dEdd-AD to snowpacks that can be treated as uniform refractive
266 media such as the air/snowpack/land columns assumed in SNICAR for model evaluation.
267 An ideal radiative treatment for snow should, however, keep the potential to include
268 refraction for further applications to snow on sea ice or ice sheets. Therefore, besides
269 these two widely used algorithms in Icepack and SNICAR, we evaluate a third algorithm
270 (section 2.3) that can be applied to layered media with either uniform or non-uniform
271 refractive indexes.

272

273 2.3. two-stream discrete-ordinate algorithm (2SD)
274 A refractive boundary also exists between the atmosphere and the ocean, and models
275 have been developed to solve the radiative transfer problems in the atmosphere-ocean
276 system using the discrete-ordinate technique (e.g. Jin and Stamnes, 1994; Lee and Liou,
277 2007). Similar to the two-stream algorithms of Toon et al., (1989) used in SNICAR, Jin
278 and Stamnes (1994) also developed their algorithm from the general equation:

279

280 $$\mu \frac{\partial I}{\partial \tau}(\tau,\mu) = I(\tau,\mu) - \frac{\varpi}{4\pi} \int_{-1}^{1} P(\tau,\mu,\mu') \, I(\tau,\mu') d\mu' - S(\tau,\mu) \tag{6}$$

281

282 Equation (6) is the azimuthally integrated version of equation (1). However, for vertically
283 inhomogeneous media like the atmosphere-ocean or sea ice, the external source term
284 $S(\tau,\mu)$ is different. Specifically, for the medium of total optical depth τ^a above the

285   refractive interface, one must consider the contribution from the upward beam reflected

286   at the refractive boundary (second term on the right-hand side):

287

288    $$S^a(\tau,\mu) = \frac{\varpi}{4\pi} F_s P(\tau,-\mu_0,\mu)\, exp\left(\frac{-\tau}{\mu_0}\right) + \frac{\varpi}{4\pi} F_s R(-\mu_0,m) P(\tau,+\mu_0,\mu) exp\left(\frac{-(2\tau^a-\tau)}{\mu_0}\right)$$

289

290   (7)

291

292   where $R(-\mu_0,m)$ is the Fresnel reflectance of radiation and m is the ratio of the

293   refractive indices of the lower to the upper medium. For the medium below the refractive

294   interface, one must account for the Fresnel transmittance $T(-\mu_0,m)$ and modify the

295   angle of beam travel in media b:

296

297    $$S^b(\tau,\mu) = \frac{\varpi}{4\pi}\frac{\mu_0}{\mu_{0n}} F_s T(-\mu_0,m) P(\tau,-\mu_0,\mu)\, exp\left(\frac{-\tau^a}{\mu_0}\right) exp\left(\frac{-(\tau-\tau^a)}{\mu_{0n}}\right)$$ (8)

298

299   where μ_{0n} is the cosine zenith angle of refracted beam incident at angle μ_0 above the

300   refractive boundary, by Snell's law:

301

302    $$\mu_{0n} = \sqrt{1-(1-\mu_0^2)/m^2}$$ (9)

303

304   For uniformly refractive media like snow on land, one can just set the refractive index m_{re}

305   equal to 1 for every layer. In this case, the Fresnel reflectance $R(-\mu_0,m)$ is 0 in equation

306   (7), the Fresenal transmittance $T(-\mu_0,m)$ is 1 in equation (8), and μ_{0n} equals to μ_0: the

307   two source terms $S^a(\tau,\mu)$ and $S^b(\tau,\mu)$ become the same and equal to the source term of

308   homogenous media given in equation (2).

309

310   For two-stream approximations of this method, analytical solutions of upward and

311   downward fluxes are coupled at each layer interface to generate 2N equations with 2N

312   unknown coefficients for any N-layer stratified column. The solutions of two-stream

313   algorithms and boundary conditions for homogenous media are well documented

314   (Sections 8.4 and 8.10 of Thomas and Stamnes, 1999). Despite the extra source terms,

315   these 2N equations can also be organized into a tridiagonal matrix similar to the method

316   of Toon et al. (1989) used in SNICAR. Flexibility and speed therefore make this two-

317   stream discrete-ordinate algorithm (hereafter, 2SD) a potentially good candidate for long-

318 term Earth system modeling. In this work, we only apply 2SD to the snowpack and note

319 that it can be applied to any uniformly or non-uniformly refractive media like snow on

320 land or sea ice, with the Delta-transform implemented to fundamental optical variables

321 (Equations 2 (a)-(c), Wiscombe and Warren, 1980).

322

323 2.4 16-stream DISORT

324 Besides the mathematical technique, the accuracy and speed of radiative transfer

325 algorithms depend on the number of angles used for flux estimation in the upward and

326 downward hemispheres. SNICAR, dEdd-AD, and 2SD use one angle to represent upward

327 flux and one angle to represent downward flux, hence they are named two-stream

328 algorithm. Lee and Liou (2007) use two upward and two downward streams. Jin and

329 Stamnes (1994) documented the solutions for any even number of streams. The

330 computational efficiency of these models is lower than that of two-stream models while

331 their accuracy is better. To quantify the accuracy of the three two-stream algorithms for

332 snow shortwave simulations, we use the 16-stream DIScrete-Odinate Radiative Transfer

333 model (DISORT) as the benchmark model (http://lllab.phy.stevens.edu/disort/) (Stamnes

334 et al., 1988).

335

336 **3. Input for radiative transfer models**

337 In this work, we focus on the performance of two-stream algorithms for pure snow

338 simulations. The inputs for these three models are the same: single-scattering properties

339 (SSPs, i.e. single-scattering albedo ϖ, asymmetry factor g, extinction coefficient σ_{ext}) of

340 snow determined by snow grain radius r, snow depth, solar zenith angle θ, solar incident

341 flux, and the albedo of underlying ground (assuming Lambertian reflectance of 0.25 for

342 all wavelengths). A Delta-transform is applied to fundamental input optical variables for

343 all simulations (Equations 2 (a)-(c), Wiscombe and Warren, 1980).

344

345 In snow, photon scattering occurs at the air-ice interface, and the absorption of photons

346 occurs within the ice crystal. The most important factor that determines snow shortwave

347 properties is the ratio of total surface area to total mass of snow grains, aka "the specific

348 surface area" (e.g. Matzl and Schneebeli, 2006, 2010). The specific surface area (β) can

349 be converted to a radiatively effective snow grain radius r:

350

351 $\beta = 3 / (r \varrho_{ice})$ (10)

352

353   where ρ_{ice} is the density of pure ice, 917 kg m^{-3}. Assuming the grains are spherical, the

354   SSPs of snow can thus be computed using Mie theory (Wiscombe, 1980) and ice optical

355   constants (Warren and Brandt, 2008). In nature, snow grains are not spherical, and many

356   studies have been carried out to quantify the accuracy of such spherical representations

357   (Grenfell and Warren, 1999; Neshyba et al., 2003; Grenfell et al., 2005). In recent years,

358   more research has been done to evaluate the impact of grain shape on snow shortwave

359   properties (Dang et al., 2016; He et al., 2017, 2018ab), and they show that non-spherical

360   snow grain shapes mainly alter the asymmetry factor. Dang et al., (2016) also point out

361   that the solar properties of a snowpack consisting of non-spherical ice grains can be

362   mimicked by a snowpack consisting of spherical grains with a smaller grain size by

363   factors up to 2.4. In this work, we still assume the snow grains are spherical, and this

364   assumption does not qualitatively alter our evaluation of the radiative transfer algorithms.

365

366   The input SSPs of snow grains are computed using Mie theory at a fine spectral

367   resolution for a wide range of ice effective radius r from 10 to 3000 μm that covers the

368   possible range of grain radius for snow on Earth (Flanner et al., 2007). The same spectral

369   SSPs were also used to derive the band-averaged SSPs of snow used in SNICAR. Note

370   Briegleb and Light (2007) refer to SSPs as inherent optical properties.

371

372   **4. Solar spectra used for the spectral integrations**

373   In climate modeling, snow albedo computation at a fine spectral resolution is expensive

374   and unnecessary. Instead of computing spectrally resolved snow albedo, wider-band solar

375   properties are more practical. For example, CESM and E3SM aggregate the narrow

376   RRTMG bands used for the atmospheric radiative transfer simulation into visible (0.2 -

377   0.7 μm) and near-IR (0.7 - 5 μm) bands. The land model and sea-ice model thus receive

378   visible and near-IR fluxes as the upper boundary condition, and return the corresponding

379   visible and near-IR albedos to atmosphere model. In practice, these bands are also

380   partitioned into direct and diffuse components. Therefore, a practical two-stream

381   algorithm should be able to simulate the direct visible, diffuse visible, direct near-IR and

382   diffuse near-IR albedos and absorptions of snow accurately.

383

384   The band albedo α is an irradiance-weighted average of the spectral albedo $\alpha(\lambda)$:

385

386     $$\alpha = \frac{\int_{\lambda 1}^{\lambda 2} \alpha(\lambda) F(\lambda) d\lambda}{\int_{\lambda 1}^{\lambda 2} F(\lambda) d\lambda}$$ (11)

387
388

389 In this work, we use the spectral irradiance $F(\lambda)$ generated by the atmospheric DISORT-
390 based Shortwave Narrowband Model (SWNB2) (Zender et al., 1997; Zender, 1999) for
391 typical clear-sky and cloudy-sky conditions of mid-latitude winter as shown in Figure
392 1(a). The total clear-sky down-welling surface flux at different solar zenith angles are
393 also given in Figure 1(b).
394
395
396 **5. Model Evaluation**
397 5.1 Spectral albedo and reflected solar flux
398 The spectral reflectance of pure deep snow computed using two-stream models and 16-
399 stream DISORT are shown in Figure 2. The snow grain radius is 100 μm - a typical grain
400 size for fresh new snow. For clear sky with direct beam source (left column), all three
401 two-stream models show good accuracy at visible wavelengths (0.3 – 0.7 μm), and within
402 this band, the snow albedo is large and close to 1. As wavelength increases, the albedo
403 diminishes in the near-IR band. Two-stream models overestimate snow albedo at these
404 wavelengths, with maximum biases of 0.013 (SNICAR and dEdd-AD) and 0.023 (2SD)
405 within wavelength 1 - 1.7 μm. For cloudy-sky cases with diffuse upper boundary
406 conditions, dEdd-AD reproduces the snow albedo at all wavelengths with the smallest
407 absolute error (< 0.005), SNICAR and 2SD both overestimate the snow albedo with
408 maximum biases > 0.04 between 1.1-1.4 μm.
409
410 In both sky conditions, the errors of snow albedo are larger at near-IR wavelengths
411 ranging from 1.0-1.7 μm, while the solar incident flux peaks at 0.5 μm then decrease as
412 wavelength increases. The largest error in reflected flux is within the 0.7-1.5 μm band for
413 SNICAR and 2SD, as shown in the 3rd row of Figure 1. dEdd-AD overestimate the direct
414 snow albedo mostly at wavelengths larger than 1.5 μm where the error in reflected flux is
415 almost negligible.
416
417 5.2 Broadband albedo and reflected solar flux
418 Integrated over the visible and near-IR wavelengths, the error in band albedos computed
419 using two-stream models for different cases are shown in Figure 3-6.
420
421 Figure 3 shows the error in direct band albedo for fixed snow grain radius of 100 μm with
422 different snow depth and solar zenith angles. As introduced in Section 2, SNICAR and
423 dEdd-AD both use delta-Eddington method to compute the visible albedo. They
424 overestimate the visible albedo for solar zenith angles smaller than 50° by up to 0.005,

425   and underestimate it for solar zenith angles larger than 50° by up to -0.01. 2SD produces
426   similar results for the visible band but at a larger solar zenith angle threshold of 75°. In
427   the near-IR band, SNICAR and 2SD overestimate the snow albedo for solar zenith angles
428   smaller than 70°, beyond this, the error in albedo increases by up to -0.1 as solar zenith
429   angle increases. dEdd-AD produces a similar error pattern with a smaller solar zenith
430   angle threshold at 60°. As snow ages, its average grain size increases. For typical old
431   melting snow of grain radius 1000 μm (Figure 4), two-stream models produce similar
432   errors of direct albedo in all bands. For snow consisting of smaller grain size, two-stream
433   models produce larger errors for visible albedo. Integrating over the entire solar band, the
434   three two-stream models evaluated show similar error patterns for direct albedo.
435
436   For a fixed solar zenith angle of 60°, the error of direct albedo for different snow depth
437   and snow grain radii are shown in Figure 5. SNICAR and dEdd-AD underestimate the
438   visible albedo in most scenarios, while 2SD overestimates the visible albedo for a larger
439   range of grain radius and snow depth. All three two-stream models tend to overestimate
440   the near-IR albedo except for shallow snow with large grain radius; the error of 2SD is
441   one order of magnitude larger than that of SNICAR and dEdd-AD.
442
443   Figure 6 is similar to Figure 5, but shows the diffuse snow albedo. In the visible band,
444   SNICAR and dEdd-AD generate similar errors in that they both underestimate the albedo
445   as snow grain size increases and snow depth decreases. 2SD overestimates the albedo
446   with a maximum error of around 0.015. In the near-IR, two-stream models tend to
447   overestimate snow albedo, while the magnitude of biases produced by SNICAR and 2SD
448   are one order larger than that of dEdd-AD with the maximum error of 0.035 generated by
449   SNICAR. As a result, the all-wave diffuse albedos computed using dEdd-AD are more
450   accurate than those computed using SNICAR and 2SD.
451
452   Figures 7, 8 and 9 show the errors in reflected shortwave flux caused by snow albedo
453   errors seen in Figures 3, 4, and 6. In general, two-stream models produce larger errors in
454   reflected direct near-IR flux (Figure 7 and 8), especially with the 2SD model: the
455   maximum overestimate of reflected near-IR flux is 6-8 Wm^{-2} for deep melting snow with
456   solar zenith angle < 30°. Errors in reflected direct visible flux are smaller (mostly within
457   ±1 Wm^{-2})for all models in most scenarios, and become larger (mostly within ±3 Wm^{-2}) as
458   snow grain size increases to 1000 μm if computed using 2SD. As shown in Figure 9, for
459   diffuse flux with solar zenith angle of 60° at TOA, SNICAR and dEdd-AD generate

460   small errors in reflected visible flux (mostly within ±1 Wm^{-2}), while 2SD always

461   overestimates reflected visible flux by up to 5 Wm^{-2}. In the near-IR, SNICAR and 2SD

462   overestimate reflected flux by as much as 10-12 Wm^{-2}; the error in reflected near-IR flux

463   produced by dEdd-AD is much smaller, mostly within ±1 Wm^{-2}.

464

465   In general, dEdd-AD produces the most accurate albedo and thus reflected flux for both

466   direct and diffuse components. SNICAR is similar to dEdd-AD for its accuracy of direct

467   albedo and flux, yet generates large error for the diffuse component. 2SD tends to

468   overestimate snow albedo and reflected flux in both direct and diffuse components and

469   shows the largest errors among three two-stream models. Although the differences

470   between algorithms are small, they can have a notable impact on snowpack melt. For

471   example, compared to dEdd-AD, SNICAR and 2SD overestimate the diffuse albedo by

472   ~0.015 for melting snow (Figure 6). In Greenland, the daily averaged downward diffuse

473   solar flux from May to September is 200 W/m^2, and the averaged cloud cover fraction is

474   80% (Figure 6, Dang et al., 2017). In this case, SNICAR and 2SD overestimate the

475   reflected solar flux by 2.4 W/m^2 per day – the amount of energy otherwise enough to melt

476   10 cm of snow water equivalent from May to September. dEdd-AD also remediates

477   compensating spectral biases (where visible and Near-IR biases are of opposite signs)

478   present in the other schemes. Those spectral biases do not affect the broadband fluxes

479   like the diffuse biases, but they nevertheless degrade proper feedbacks between snow/ice

480   reflectance and heating."

481

482   5.3 Band absorption of solar flux

483   Figure 10 shows absorption profiles of shortwave flux computed using the 16-stream

484   DISORT model, with errors in absorbed fractional solar flux computed using two-stream

485   models. The snowpack is 10-cm deep and is divided into 5 layers, each 2-cm thick. The

486   snow grain radius is set to 100 μm. The figure shows fractional absorption for snow

487   layers 1-4 and the underlying ground with an albedo of 0.25.

488

489   As shown in the first column of Figure 10, for new snow with a radius of 100 μm, most

490   solar absorption occurs in the top 2-cm snow layer, where roughly 10% and 15% of

491   diffuse and direct near-IR flux are absorbed and dominate the solar absorption within the

492   snowpack. In the second layer (2-4 cm), the absorption of solar flux is less than 1% and

493   gradually decreases within the interior layers. The underlying ground absorbs roughly 2%

494   of solar flux, mostly visible flux that penetrates the snowpack more efficiently. As snow

495 ages and snow grain grows, photons penetrate deeper into the snowpack. For typical old
496 melting snow with a radius of 1000 μm, most solar absorption still occurs in the top 2-cm
497 snow layer, where roughly 20% and 14% of diffuse and direct near-IR flux are absorbed.
498 The second snow layer (2-4 cm) absorbs more near-IR solar flux by roughly 2%. More
499 photons can penetrate through the snowpack, and results in a high fractionally absorption
500 by the underlying ground, especially for the visible band. As snow depth increase, the
501 ground absorption will decrease for both snow radii.
502
503 Comparing to 16-stream DISORT, two-stream models underestimate the column solar
504 absorptions for new snow, and they overestimate them for old snow, especially for the
505 surface snow layer and the underground. Overall, dEdd-AD gives the most accurate
506 absorption profiles among the three two-stream models, especially for new snow.
507

508 **6. Correction for direct albedo for large solar zenith angles**
509
510 It has been pointed out in previous studies that the two-stream approximations become
511 poor as solar zenith angle approaches 90° (e.g. Wiscombe 1977, Warren 1982). As shown
512 in Figures 3 and 4, all three two-stream models underestimate the direct snow albedo for
513 large solar zenith angles. In the visible band, when the snow grain size is small, the error
514 in direct albedo is almost negligible (Figure 3); while as snow ages and snow grains
515 become larger, the error increases yet remains low if the snow is deep (Figure 4). In the
516 near-IR, the biases of albedo are also larger for larger snow grain radii. For a given snow
517 size, the magnitudes of such biases are almost independent of snow depth, and mainly
518 determined by the solar zenith angle. In general, the errors of all-wave direct albedo are
519 mostly contributed by the errors of near-IR albedo, especially for optically thick
520 snowpacks (i.e., semi-infinite), because the errors of direct albedo in the visible are
521 negligible compared with those in the near-IR. To improve the performance of two-
522 stream algorithms, we develop a parameterization that corrects the underestimated near-
523 IR snow albedo at large zenith angles.
524

525 Figure 11 shows the direct near-IR albedo and fractional absorption of 2-meter thick
526 snowpacks consisting of grains with radius 100 μm and 1000 μm, computed using two-
527 stream algorithms and 16-stream DISORT. For solar zenith angles > 75°, two-stream
528 models underestimate snow albedo and overestimate solar absorption within the
529 snowpack, mostly in the top 2-cm of snow, and the differences among the three two-
530 stream models are small. In Section 5, we have shown that dEdd-AD produces the most

531 accurate snow albedo in general. With anticipated wide application of dEdd-AD, we
532 develop the following parameterization to adjust its low biases in computed near-IR
533 direct albedo.

534

535 We define and compute R_{75+} as the ratio of direct semi-infinite near-IR albedo computed
536 using 16-stream DISORT ($\alpha_{16\text{-}DISORT}$) to that computed using dEdd-AD ($\alpha_{dEdd\text{-}AD}$), for
537 solar zenith angle $> 75°$. This ratio is shown in Figure 11 (c) and can be parameterized as
538 a function of snow grain radius (r, unit in meter) and the cosine of incident solar zenith
539 angle (μ_0), as shown in Figure 11(c):

540

541 $$R_{75+} = \frac{\alpha_{16-DISORT}}{\alpha_{dEdd-AD}} = c_1(\mu_0)log_{10}(r) + c_0(\mu_0), \ for \, \mu_0 < 0.26, \, i.e. \ \theta_0 > 75° \qquad (12)$$

542

543 where coefficients c_1 and c_0 are polynomial functions of μ_0, as shown in Figure 11(d):

544

545 $$c_1(\mu_0) = 1.304\mu_0^2 - 0.631\mu_0 + 0.086 \qquad (13a)$$

546 $$c_0(\mu_0) = 6.807\mu_0^2 - 3.338\mu_0 + 1.467 \qquad (13b)$$

547

548 Since two-stream models always underestimate snow albedo, R_{75+} always exceeds 1
549 (Figure 11c). We can then adjust the direct near-IR snow albedo ($\alpha_{dEdd\text{-}AD}$) and direct
550 near-IR solar absorption ($Fabs_{dEdd\text{-}AD}$) by snow computed using dEdd-AD with ratio
551 R_{75+}:

552

553 $$\alpha_{dEdd-AD}^{adjust} = R_{75+}\alpha_{dEdd-AD} \qquad (14a)$$

554

555 $$Fabs_{dEdd-AD}^{adjust} = Fabs_{dEdd-AD} - (R_{75+} - 1)\alpha_{dEdd-AD}F_{nir} \qquad (14b)$$

556

557 where F_{nir} is the direct near-IR flux. This adjustment reduces the error of near-IR albedo
558 from negative 2-10% to within $\pm 0.5\%$ for solar zenith angles larger than 75°, and for
559 grain radii ranging from 30-1500 μm (Figure 12). Errors in broadband direct albedo are
560 therefore also reduced to < 0.01. The direct near-IR flux absorbed by the snowpack
561 decreases after applying this adjustment.

562

563   When the solar zenith angle exceeds 75°, our model adjusts the computed direct near-IR

564   albedo αdEdd-AD by the ratio *R75+* following equations 12-14a and reduces direct near-

565   IR absorption following equation 14b. If snow is divided into multiple layers, we assume

566   all decreased near-IR absorption (2nd term on the right-hand side, equation 14b) is

567   confined within the top layer. This assumption is fairly accurate for the near-IR band,

568   since most absorption occurs at the surface of the snowpack (Figures 10 and 11). As

569   discussed previously, this parameterization is developed based on albedo computed using

570   dEdd-AD. For models that do not use dEdd-AD but SNICAR and 2SD, the same

571   adjustment still applies given the small differences of near-IR direct albedo computed

572   using two-stream models (Figure 11). For models that adopt other radiative transfer

573   algorithms it is best for the developers to examine their model against a benchmark

574   model such as 16-stream DISORT or two-stream models discussed in this work before

575   applying this correction.

576

577   Although the errors of direct near-IR albedos are large for large solar zenith angles, the

578   absolute error in reflected shortwave flux is small (Figures 7 and 8) as the down-welling

579   solar flux reaches snowpack decreases as solar zenith angle increases (Figures 1(b)).

580   However, such small biases in flux can be important for high latitudes where the solar

581   zenith angle is large for many days in late winter and early spring.

582

583 7. Implementation of snow radiative transfer model in Earth system models
584

585   ESMs often use band-averaged SSPs of snow and aerosols for computational efficiency,

586   rather than using brute-force integration of spectral solar properties across each band (per

587   equation 11). Besides using different radiative transfer approximations, SNICAR and

588   dEdd-AD also adopt different methods to derive the band-averaged SSPs of snow for

589   different band schemes.

590

591   In SNICAR, snow solar properties are computed for 5 bands: one visible band (0.3 -

592   0.7μm), and four near-IR bands (0.7 - 1 μm, 1 – 1.2 μm, 1.2 – 1.5 μm, and 1.5 – 5 μm).

593   The solar properties of four subdivided near-IR bands are combined by fixed ratios to

594   compute the direct/diffuse near-IR snow properties. These two sets of ratios are derived

595   offline based on the incident solar spectra of typical of mid-latitude winter for clear and

596   cloudy-sky conditions clear sky and cloudy sky, respectively (Figure 1(a)).

597

598   The band-averaged SSPs of snow grains are computed following the Chandrasekhar
599   Mean approach (Thomas and Stamnes, 1999, their Equation 9.27; Flanner et al., 2007).
600   Specifically, spectral SSPs of snow grains are weighted into bands according to surface
601   incident solar flux typical of mid-latitude winter for clear and cloudy sky conditions. In
602   addition, the single-scattering albedo $\varpi(\lambda)$ of ice grains are also weighted by the
603   hemispheric albedo $\alpha(\lambda)$ of an optically thick snowpack:

604

605    $$\varpi(\bar{\lambda}) = \frac{\int_{\lambda_1}^{\lambda_2} \varpi(\lambda)F(\lambda)\alpha(\lambda)d\lambda}{\int_{\lambda_1}^{\lambda_2} F(\lambda)\alpha(\lambda)d\lambda} \qquad (15a)$$

606    $$g(\bar{\lambda}) = \frac{\int_{\lambda_1}^{\lambda_2} g(\lambda)F(\lambda)d\lambda}{\int_{\lambda_1}^{\lambda_2} F(\lambda)\alpha(\lambda)d\lambda} \qquad (15b)$$

607    $$\sigma_{ext}(\bar{\lambda}) = \frac{\int_{\lambda_1}^{\lambda_2} \sigma_{ext}(\lambda)F(\lambda)d\lambda}{\int_{\lambda_1}^{\lambda_2} F(\lambda)\alpha(\lambda)d\lambda} \qquad (15c)$$

608

609   Two sets of snow band-averaged SSPs are generated for all grain radii, suitable for direct
610   and diffuse light, respectively. For each modeling step and band, SNICAR is called twice
611   to compute the direct and diffuse snow solar properties.

612

613   In dEdd-AD, the snow-covered sea ice properties are computed for 3 bands: one visible
614   band (0.3 – 07 μm), and two near-IR bands (0.7 – 1.19 μm and 1.19 – 5 μm). The solar
615   proprieties of these two near-IR bands are combined using ratios w_{nir1} and w_{nir2} for 0.7-1
616   .19 μm and 1.19-5 μm, depending on the fraction of direct near-IR flux f_{nidr}:

617

618    $$w_{nir1} = 0.67 + 0.11 * (1 - f_{nidr}) \qquad (16a)$$
619    $$w_{nir2} = 1 - w_{nir1} \qquad (16b)$$

620

621   The band SSPs of snow are derived by integrating the spectral SSPs and the spectral
622   surface solar irradiance measured in the Arctic under mostly clear sky.

623

624    $$\varpi(\bar{\lambda}) = \int_{\lambda_1}^{\lambda_2} \varpi(\lambda)F(\lambda)d\lambda \qquad (17a)$$

625    $$g(\bar{\lambda}) = \int_{\lambda_1}^{\lambda_2} g(\lambda)F(\lambda)d\lambda \qquad (17b)$$

626    $$\sigma_{ext}(\bar{\lambda}) = \int_{\lambda_1}^{\lambda_2} \sigma_{ext}(\lambda)F(\lambda)d\lambda \qquad (17c)$$

627

628 In addition, the band-averaged single-scattering albedo $\varpi(\bar{\lambda})$ is also increased to $\varpi(\bar{\lambda})'$

629 until the band albedo computed using averaged SSPs matches the band albedo $\bar{\alpha}$ within

630 0.0001, where $\bar{\alpha}$ is:

631

632 $$\bar{\alpha} = \int_{\lambda_1}^{\lambda_2} \alpha(\lambda)F(\lambda)d\lambda \tag{18}$$

633

634 dEdd-AD adopts this single set of band SSPs for both direct and diffuse computations. In

635 practice, the physical snow grain radius r is adjusted to a radiatively equivalent radius r_{eqv}

636 based on the fraction of direct flux in the near-IR band (f_{nidr}):

637

638 $$r_{eqv} = (f_{nidr} + 0.8(1 - f_{nidr}))r \tag{19}$$

639

640 This r_{eqv} and the corresponding snow SSPs are then used in the radiative transfer

641 calculation. The computed direct and diffuse solar properties alone are less accurate,

642 while the combined all-sky broadband solar properties agree with SNICAR (Briegleb and

643 Light, 2007). As a result, for each modeling step and band, dEdd-AD radiative transfer

644 subroutine is called only once to compute both the direct and diffuse snow solar

645 properties simultaneously.

646

647 SNICAR and dEdd-AD also use different approaches to avoid numerical singularities. In

648 SNICAR, singularities occur when the denominator of term $C_n^{\pm}$ in equation (3) equals to

649 zero (i.e., $\gamma^2 - 1/\mu_0^2 = 0$), where γ is determined by the approximation method and SSPs

650 of snow, and μ_0 is the cosine of the solar zenith angle (Equations 23 and 24, Toon et al.,

651 1989). When such a singularity is detected, SNICAR will shift μ_0 by + 0.02 or -0.02 to

652 obtain physically realistic radiative properties. In the dEdd-AD algorithm, singularities

653 arise only when $\mu_0 = 0$ (Equation 4). Therefore, in practice, for $\mu_0 < 0.01$, dEdd-AD

654 computes the sea-ice solar properties for $\mu_0 = 0.01$ to avoid unphysical results.

655

656 **8. Towards a unified radiative transfer model for snow, sea ice, and land ice.**
657
658

659   Based on the inter-comparison of three two-stream algorithms and their implementations
660   in ESMs, we formulated the following surface shortwave radiative transfer
661   recommendations for an accurate, fast, and consistent treatment for snow on land, land
662   ice, and sea ice in ESMs:

663

664   First, the two-stream delta-Eddington adding-doubling algorithm by Briegleb and Light
665   (2007) is unsurpassed as a radiative transfer core. The evaluation in Section 5 shows that
666   this algorithm produces the least error for snow albedo and solar absorption within
667   snowpack, especially under overcast skies. This algorithm applies well to both uniformly
668   refractive media such as snow on land, and to non-uniformly refractive media, such as
669   bare/snow-covered/ponded sea ice and bare/snow-covered land ice. Numerical
670   singularities occur only rarely (when $\mu_0 = 0$) and are easily avoided in model
671   implementations. Among the three two-stream algorithms discussed here, dEdd-AD is
672   also the most efficient one as it takes only ~2/3 of the time of SNICAR and 2SD to
673   compute solar properties of multi-layer snowpacks.

674

675   Second, any two-stream cryospheric radiative transfer model can incorporate the
676   parameterization described in Section 6 to adjust the low bias of direct near-IR snow
677   albedo and high bias of direct near-IR solar absorption in snow, for solar zenith angles
678   larger than 75°. These biases are persistent across all two-stream algorithms discussed in
679   this work, and should be corrected for snow-covered surfaces. Alternatively, adopting a
680   4-stream approximation would reduce or eliminate such biases, though at considerable
681   expense in computational efficiency.

682

683   Third, in a cryospheric radiative transfer model, one should prefer physically based
684   parameterizations that are extensible and convergent (e.g., with increasing spectral
685   resolution) for the band-averaged SSPs and size distribution of snow. Although the
686   treatments used in SNICAR and dEdd-AD are both practical since they both reproduce
687   the narrowband solar properties with carefully derived band-averaged inputs as discussed
688   in Section 7, the snow treatment used in SNICAR is more physically based and
689   reproducible since it does not rely on subjective adjustment and empirical coefficients as
690   used in dEdd-AD. Specifically, the empirical adjustment to snow grain radius
691   implemented in dEdd-AD may not always produce compensating errors. For example, in
692   snow containing light-absorbing impurities such adjustment may also lead to biases in
693   aerosol absorption since the albedo reduction caused by light-absorbing particles does not
694   linearly depend on snow grain radius (Dang et al., 2015). For further model development

695   incorporating non-spherical snow grain shapes (Dang et al., 2016; He et al., 2018ab),
696   such adjustment on grain radius may fail as well. Moreover, SNICAR computes the snow
697   properties for four near-IR bands, which helps capture the spectral variation of albedo
698   (Figure 2) and therefore better represents near-IR solar properties. It is also worth noting
699   that unlike the radiative core of dEdd-AD, SNICAR is actively maintained with
700   numerous modifications and updates in the past decade (e.g. Flanner et al., 2012; He et
701   al., 2018b). Snow radiative treatments that follow SNICAR conventions for SSPs may
702   take advantage of these updates. Note that any radiative core that follows SNICAR SSP
703   conventions must be called twice to compute diffuse and direct solar properties,
704   respectively.

705

706   Fourth, a surface cryospheric radiative transfer model should flexibly accommodate
707   coupled simulations with distinct atmospheric and surface spectral grids. Both the 5-band
708   scheme used in SNICAR and the 3-band scheme used in dEdd-AD separate the visible
709   from near-IR spectrum at 0.7 μm. This boundary aligns with the Community
710   Atmospheric Model's original radiation bands (CAM; Neale et al., 2012), though not
711   with the widely used Rapid Radiative Transfer Model (RRTMG; Iacono et al., 2008)
712   which places 0.7 μm squarely in the middle of a spectral band. A mismatch in spectral
713   boundaries between atmospheric and surface radiative transfer schemes can require an
714   ESM to unphysically apportion energy from the straddled spectral bin when coupling
715   fluxes between surface and atmosphere. The spectral grids of surface and atmosphere
716   radiation need not be identical so long as the coarser grid shares spectral boundaries with
717   the finer grid. In practice maintaining a portable cryospheric radiative module such as
718   SNICAR requires a complex offline toolchain (Mie solver, spectral refractive indices for
719   air, water, ice, and aerosols, spectral solar insolation for clear and cloudy skies) to
720   compute, integrate, and rebin SSPs. Aligned spectral boundaries between surface and
721   atmospheric would simplify the development of efficient and accurate radiative transfer
722   for the coupled Earth system.

723

724   Last, it is important to note that, although we only examine the performance of the dEdd-
725   AD for pure snow in this work, this algorithm can be applied to the surface solar
726   calculation of all cryospheric components with or without light-absorbing particles
727   present. First, Briegleb and Light (2007) proved its accuracy for simulating ponded/bare
728   sea-ice solar properties against observations and a Monte Carlo radiation model. Second,
729   In CESM and E3SM, the radiative transfer simulation of snow on land ice is carried out
730   by SNICAR with prescribed land ice albedo. Adopting the dEdd-AD radiative core in

731   SNICAR will permit these ESMs to couple the snow and land ice as a non-uniformly
732   refractive column for more accurate solar computations since bare/snow-covered/ponded
733   land ice is physically similar to bare/snow-covered/ponded sea ice, and the latter is
734   already treated well by dEdd-AD radiative transfer core. Third, adding light-absorbing
735   particles in snow will not change our results qualitatively. Both dEdd-AD and SNICAR
736   simulate the impact of light-absorbing particles (black carbon and dust) on snow and/or
737   sea ice using self-consistent particle SSPs that follow the SNICAR convention (e.g.,
738   Flanner et al., 2007; Holland et al. 2012). These particles are assumed to be either
739   internally or externally mixed with snow crystals; the combined SSPs of mixtures (e.g.
740   Appendix A of Dang et al., 2015) are then used as the inputs for radiative transfer
741   calculation. The adoption of dEdd-AD radiative transfer algorithm in SNICAR, and the
742   implementation of SNICAR snow SSPs in dEdd-AD enables a consistent simulation of
743   the radiative effects of light-absorbing particles in the cryosphere across ESM
744   components.
745
746   In summary, this inter-comparison and evaluation has shown multiple ways that the solar
747   properties of cryospheric surfaces can be improved in the current generation of ESMs.
748   We have merged these findings into a hybrid model SNICAR-AD, which is primarily
749   composed of the radiative transfer scheme of dEdd-AD, 5-band snow/aerosol SSPs of
750   SNICAR, and the parameterization to correct for snow albedo biases when solar zenith
751   angle exceeds 75°. This hybrid model can be applied to snow on land, land ice, and sea
752   ice to produce consistent shortwave radiative properties for snow-covered surfaces across
753   the Earth system. With the evolving and further understanding of snow and aerosol
754   physics and chemistry, the adoption of this hybrid model will obviate the effort to modify
755   and maintain separate optical variable input files used for different model components.
756
757   SNICAR-AD is now implemented in both the sea-ice (MPAS-seaice) and land (ELM)
758   components of E3SM. More simulations and analyses are underway to examine its
759   impact on E3SM model performance and simulated climate. The results are however
760   beyond the scope of this work and will be thoroughly discussed in a future paper.
761

762   **9. Conclusions**
763   In this work, we aim to improve and unify the solar radiative transfer calculations for
764   snow on land and snow on sea ice in ESMs by evaluating the following two-stream
765   radiative transfer algorithms: the two-stream delta-Eddington adding-doubling algorithm
766   dEdd-AD implemented in sea-ice model Icepack/CICE/MPAS-seaice, the two-stream

767   delta-Eddington and two-stream delta-Hemispheric-Mean algorithms implemented in
768   snow model SNICAR, and a two-stream delta-Discrete-Ordinate algorithm. Among these
769   three models, the dEdd-AD produces the most accurate snow albedo and solar absorption
770   (Section 5). All two-stream models underestimate near-IR snow albedo and overestimate
771   near-IR absorption when solar zenith angles are larger than 75°, which can be adjusted by
772   a parameterization we developed (Section 6). We compared the implementations of
773   radiative transfer cores in SNICAR and dEdd-AD (Section 7) and recommended a
774   consistent and hybrid shortwave radiative model SNICAR-AD for snow-covered surfaces
775   across ESMs (Section 8). Improved treatment of surface cryospheric radiative properties
776   in the thermal infrared has recently been shown to remediate significant climate
777   simulation biases in Polar Regions (Huang et al., 2018). It is hoped that adoption of
778   improved and consistent treatments of solar radiative properties for snow-covered
779   surfaces as described in this study will further remediate simulation biases in snow-
780   covered regions.
781

Data availability. The data and models are available upon request to Cheng Dang (cdang5@uci.edu). SNICAR and dEdd-AD radiative transfer core can be found at https://github.com/E3SM-Project/E3SM.

Competing interests. The authors declare that they have no conflict of interest.

Acknowledgments. The authors thank Prof. Stephen G. Warren and Prof. Qiang Fu for insightful discussions on radiative transfer algorithms. The authors thank Dr. Adrian Turner for instructions on installing and running MPAS-seaice. The authors thank Dr. David Bailey and one anonymous reviewer for their constructive comments that improved our manuscript. This research is supported as part of the Energy Exascale Earth System Model (E3SM) project, funded by the U.S. Department of Energy, Office of Science, Office of Biological and Environmental Research, with funding number DE-SC0012998.

References

Aoki, T., Kuchiki, K., Niwano, M., Kodama, Y., Hosaka, M. and Tanaka, T.: Physically based snow albedo model for calculating broadband albedos and the solar heating profile in snowpack for general circulation models. Journal of Geophysical Research, 116, D11114, https://doi.org/10.1029/2010JD015507, 2011.

Bøggild, C.E., Brandt, R.E., Brown, K.J. and Warren, S.G.: The ablation zone in northeast Greenland: ice types, albedos and impurities. Journal of Glaciology, 56, 101-113, pp.101-113, https://doi.org/10.3189/002214310791190776, 2010.

Brandt, R.E., Warren, S.G., Worby, A.P. and Grenfell, T.C.: Surface albedo of the Antarctic sea ice zone. Journal of Climate, 18(17), pp.3606-3622. https://doi.org/10.1175/JCLI3489.1 2005.

Briegleb, P. and Light, B.: A Delta-Eddington mutiple scattering parameterization for solar radiation in the sea ice component of the community climate system model, 2007.

Dang, C. and Hegg, D.A.: Quantifying light absorption by organic carbon in Western North American snow by serial chemical extractions. Journal of Geophysical Research, 119(17), pp.10-247. https://doi.org/10.1002/2014JD022156, 2014.

Dang, C., Fu, Q. and Warren, S.G., 2016. Effect of snow grain shape on snow albedo. Journal of the Atmospheric Sciences, 73(9), pp.3573-3583. https://doi.org/10.1175/JAS-D-15-0276.1, 2016.

Dang, C., Brandt, R.E. and Warren, S.G.: Parameterizations for narrowband and broadband albedo of pure snow and snow containing mineral dust and black carbon. Journal of Geophysical Research: Atmospheres, 120(11), pp.5446-5468, https://doi.org/10.1002/2014JD022646, 2015.

Dang, C., Warren, S.G., Fu, Q., Doherty, S.J., Sturm, M. and Su, J.: Measurements of light-absorbing particles in snow across the Arctic, North America, and China:

823   Effects on surface albedo. Journal of Geophysical Research: Atmospheres, 122(19),
824   pp.10-149. https://doi.org/10.1002/2017JD027070, 2017.

825   Doherty, S.J., Hegg, D.A., Johnson, J.E., Quinn, P.K., Schwarz, J.P., Dang, C. and
826   Warren, S.G.: Causes of variability in light absorption by particles in snow at sites in
827   Idaho and Utah. Journal of Geophysical Research: Atmospheres, 121(9), pp.4751-
828   4768. https://doi.org/10.1002/2015JD024375, 2016.

829   Doherty, S.J., Warren, S.G., Grenfell, T.C., Clarke, A.D. and Brandt, R.E.: Light-
830   absorbing impurities in Arctic snow. Atmospheric Chemistry and Physics. 10(23),
831   pp.11647-11680. https://doi.org/10.5194/acp-10-11647-2010, 2010.

832   Doherty, S.J., Dang, C., Hegg, D.A., Zhang, R. and Warren, S.G.: Black carbon and other
833   light-absorbing particles in snow of central North America. Journal of Geophysical
834   Research: Atmospheres, 119(22), pp.12-807, https://doi.org/10.1002/2014JD022350,
835   2014.

836   Flanner, M.G. and Zender, C.S.: Snowpack radiative heating: Influence on Tibetan
837   Plateau climate. Geophysical Research Letters, 32(6).
838   https://doi.org/10.1029/2004GL022076, 2005.

839   Flanner, M.G., Zender, C.S., Randerson, J.T. and Rasch, P.J.: Present-day climate forcing
840   and response from black carbon in snow. Journal of Geophysical Research:
841   Atmospheres, 112(D11). https://doi.org/10.1029/2006JD008003, 2007.

842   Flanner, M.G., Liu, X., Zhou, C., Penner, J.E. and Jiao, C.: Enhanced solar energy
843   absorption by internally-mixed black carbon in snow grains. Atmospheric Chemistry
844   and Physics, 12(10), pp.4699-4721. https://doi.org/10.5194/acp-12-4699-2012, 2012.

845   Gardner, A.S. and Sharp, M.J.: A review of snow and ice albedo and the development of
846   a new physically based broadband albedo parameterization. Journal of Geophysical
847   Research: Earth Surface, 115(F1). https://doi.org/10.1029/2009JF001444, 2010.

848   Grenfell, T.C., Neshyba, S.P. and Warren, S.G.: Representation of a nonspherical ice
849   particle by a collection of independent spheres for scattering and absorption of
850   radiation: 3. Hollow columns and plates. Journal of Geophysical Research:
851   Atmospheres, 110(D17). https://doi.org/10.1029/2005JD005811, 2005.

852   He, C., Liou, K.N., Takano, Y., Yang, P., Qi, L. and Chen, F.: Impact of grain shape and
853   multiple black carbon internal mixing on snow albedo: Parameterization and radiative
854   effect analysis. Journal of Geophysical Research: Atmospheres, 123(2), pp.1253-
855   1268. https://doi.org/10.1002/2017JD027752, 2018a.

856   He, C., Flanner, M.G., Chen, F., Barlage, M., Liou, K.N., Kang, S., Ming, J. and Qian,
857   Y.: Black carbon-induced snow albedo reduction over the Tibetan Plateau:
858   uncertainties from snow grain shape and aerosol–snow mixing state based on an
859   updated SNICAR model. Atmospheric Chemistry and Physics, 18, pp.11507-11527.
860   https://doi.org/10.5194/acp-18-11507-2018, 2018b.

861   He, C., Takano, Y., Liou, K.N., Yang, P., Li, Q. and Chen, F.: Impact of Snow Grain
862   Shape and Black Carbon–Snow Internal Mixing on Snow Optical Properties:
863   Parameterizations for Climate Models. Journal of Climate, 30(24), pp.10019-10036.
864   https://doi.org/10.1175/JCLI-D-17-0300.1, 2017.

865   Holland, M.M., Bailey, D.A., Briegleb, B.P., Light, B. and Hunke, E.: Improved sea ice
866   shortwave radiation physics in CCSM4: The impact of melt ponds and aerosols on
867   Arctic sea ice. Journal of Climate, 25(5), pp.1413-1430. https://doi.org/10.1175/JCLI-
868   D-11-00078.1, 2012.

869   Huang, X., Chen, X., Flanner, M., Yang, P., Feldman, D. and Kuo, C.: Improved
870   representation of surface spectral emissivity in a global climate model and its impact
871   on simulated climate. Journal of Climate, 31(9), pp.3711-3727.
872   https://doi.org/10.1175/JCLI-D-17-0125.1, 2018.

873   Hunke, E. C., Lipscomb, W. H., Turner, A. K., Jeffery, N., and Elliott, S.: CICE: the Los
874   Alamos Sea Ice Model Documentation and Software User's Manual Version 4.1 LA-
875   CC-06-012. T-3 Fluid Dynamics Group, Los Alamos National Laboratory 675. 2010.

876   Iacono, M.J., Delamere, J.S., Mlawer, E.J., Shephard, M.W., Clough, S.A. and Collins,
877   W.D.: Radiative forcing by long‐lived greenhouse gases: Calculations with the AER
878   radiative transfer models. Journal of Geophysical Research: Atmospheres, 113(D13),
879   https://doi.org/10.1029/2008JD009944, 2008.

880   Jin, Z. and Stamnes, K.: Radiative transfer in nonuniformly refracting layered media:
881   atmosphere–ocean system. Applied Optics, 33(3), pp.431-442.
882   https://doi.org/10.1364/AO.33.000431, 1994.

883   Kuipers Munneke, P., Van den Broeke, M.R., Lenaerts, J.T.M., Flanner, M.G., Gardner,
884   A.S. and Van de Berg, W.J.: A new albedo parameterization for use in climate
885   models over the Antarctic ice sheet. Journal of Geophysical Research: Atmospheres,
886   116(D5). https://doi.org/10.1029/2010JD015113, 2011.

887   Lee, W.L. and Liou, K.N.: A coupled atmosphere–ocean radiative transfer system using
888   the analytic four-stream approximation. Journal of the Atmospheric Sciences, 64(10),
889   pp.3681-3694. https://doi.org/10.1175/JAS4004.1, 2007.

890   Liang, S., Fang, H., Chen, M., Shuey, C.J., Walthall, C., Daughtry, C., Morisette, J.,
891   Schaaf, C. and Strahler, A.: Validating MODIS land surface reflectance and albedo
892   products: Methods and preliminary results. Remote sensing of environment, 83(1-2),
893   pp.149-162. https://doi.org/10.1016/S0034-4257(02)00092-5, 2002.

894   Light, B., Grenfell, T. C. and Perovich, D.K.: Transmission and absorption of solar
895   radiation by Arctic sea ice during the melt season. Journal of Geophysical Research:
896   Oceans 113, no. C3, https://doi.org/10.1029/2006JC003977, 2008.

897   Light, B., Perovich, D.K., Webster M.A., Polashenski, C., and Dadic, R.: Optical
898   properties of melting first-year Arctic sea ice. Journal of Geophysical Research:
899   Oceans 120, no. 11: 7657-7675, https://doi.org/10.1002/2015JC011163, 2015.

900   Marshall, S. and Oglesby, R.J.: An improved snow hydrology for GCMs. Part 1: Snow
901   cover fraction, albedo, grain size, and age. Climate Dynamics, 10(1-2), pp.21-37.
902   https://doi.org/10.1007/BF00210334, 1994.

903   Marshall, S.E.: A Physical Parameterization of Snow Albedo for Use in Climate Models,
904   NCAR Cooperative Thesis 123, National Center for Atmospheric Research,
905   Boulder, CO, 175 pp. 1989.

Matzl, M. and Schneebeli, M.: Measuring specific surface area of snow by near-infrared photography. Journal of Glaciology, 52(179), pp.558-564. https://doi.org/10.3189/172756506781828412, 2006.

Matzl, M. and Schneebeli, M.: Stereological measurement of the specific surface area of seasonal snow types: Comparison to other methods, and implications for mm-scale vertical profiling. Cold Regions Science and Technology, 64(1), pp.1-8. https://doi.org/10.1016/j.coldregions.2010.06.006, 2010.

Meador, W.E. and Weaver, W.R.: Two-stream approximations to radiative transfer in planetary atmospheres: A unified description of existing methods and a new improvement. Journal of the Atmospheric Sciences, 37(3), pp.630-643. https://doi.org/10.1175/1520-0469(1980)037<0630:TSATRT>2.0.CO;2, 1980.

Mlawer, E.J. and Clough, S.A.: On the extension of rapid radiative transfer model to the shortwave region. In Proceedings of the 6th Atmospheric Radiation Measurement (ARM) Science Team Meeting, US Department of Energy, CONF-9603149, 223–226. 1997.

Neale, Richard B., Chen, C.-C., Gettelman, A., Lauritzen, P. H., Park, S., Williamson, D. L., Conley, A. J., Garcia, R., Kinnison, D., Lamarque, J. F., and Marsh, D.: Description of the NCAR community atmosphere model (CAM 5.0). NCAR Tech. Note NCAR/TN-486+ STR 1, no. 1: 1-12. 2010.

Neshyba, S.P., Grenfell, T.C. and Warren, S.G.: Representation of a nonspherical ice particle by a collection of independent spheres for scattering and absorption of radiation: 2. Hexagonal columns and plates. Journal of Geophysical Research: Atmospheres, 108(D15). https://doi.org/10.1029/2002JD003302, 2003.

Perovich, D. K.: The optical properties of sea ice (No. MONO-96-1). COLD REGIONS RESEARCH AND ENGINEERING LAB HANOVER NH. 1996.

Stamnes, K., Tsay, S.C., Wiscombe, W. and Jayaweera, K.: Numerically stable algorithm for discrete-ordinate-method radiative transfer in multiple scattering and emitting layered media. Applied optics, 27(12), pp.2502-2509. https://doi.org/10.1364/AO.27.002502, 1988.

Thomas, G.E. and K. Stamnes (1999), Radiative transfer in the atmosphere and ocean. Cambridge University Press.

Toon, O. B., McKay, C. P., Ackerman, T. P., and Santhanam, K.: Rapid calculation of radiative heating rates and photodissociation rates in inhomogeneous multiple scattering atmospheres, J. Geophys. Res., 94(D13), 16,287–16,301. https://doi.org/10.1029/JD094iD13p16287, 1989.

Turner, A.K., Lipscomb, W.H., Hunke, E.C., Jacobsen, D.W., Jeffery, N., Ringler, T.D. and Wolfe, J.D.: MPAS-Seaice: a new variable resolution sea-ice model. J. Adv. Model Earth Sy., in preparation., 2018.

Wang, X., Doherty, S.J. and Huang, J.: Black carbon and other light-absorbing impurities in snow across Northern China. Journal of Geophysical Research: Atmospheres, 118(3), pp.1471-1492. https://doi.org/10.1029/2012JD018291, 2013.

947 Warren, S. G.: Optical properties of snow. Reviews of Geophysics 20, no. 1: 67-89.
948   https://doi.org/10.1029/RG020i001p00067,1982.

949 Warren, S.G. and Wiscombe, W.J.: A model for the spectral albedo of snow. II: Snow
950   containing atmospheric aerosols. Journal of the Atmospheric Sciences, 37(12),
951   pp.2734-2745.https://doi.org/10.1175/1520-
952   0469(1980)037<2734:AMFTSA>2.0.CO;2, 1980

953 Warren, S.G. and Brandt, R.E.: Optical constants of ice from the ultraviolet to the
954   microwave: A revised compilation. Journal of Geophysical Research: Atmospheres,
955   113(D14). https://doi.org/10.1029/2007JD009744, 2008.

956 Warren, S.G. and Wiscombe, W.J.: Dirty snow after nuclear war. Nature, 313(6002),
957   p.467. https://doi.org/10.1038/313467a0, 1985.

958 Wiscombe, W. J.: The delta-Eddington approximation for a vertically inhomogeneous
959   atmosphere, NCAR Tech. Note TN-140_STR [NTIS P6270618]. 1977.

960 Wiscombe, W.J.: Improved Mie scattering algorithms. Applied optics, 19(9), pp.1505-
961   1509. https://doi.org/10.1364/AO.19.001505,1980.

962 Wiscombe, W.J. and Warren, S.G.: A model for the spectral albedo of snow. I: Pure
963   snow. Journal of the Atmospheric Sciences, 37(12), pp.2712-2733.
964   https://doi.org/10.1175/1520-0469(1980)037<2712:AMFTSA>2.0.CO;2, 1980.

965 Zender, C.S.: Global climatology of abundance and solar absorption of oxygen collision
966   complexes. Journal of Geophysical Research: Atmospheres, 104(D20), pp.24471-
967   24484. https://doi.org/10.1029/1999JD900797, 1999.

968 Zender, C.S., Bush, B., Pope, S.K., Bucholtz, A., Collins, W.D., Kiehl, J.T., Valero, F.P.
969   and Vitko Jr, J.: Atmospheric absorption during the atmospheric radiation
970   measurement (ARM) enhanced shortwave experiment (ARESE). Journal of
971   Geophysical Research: Atmospheres, 102(D25), pp.29901-29915.
972   https://doi.org/10.1029/97JD01781, 1997.

973

974 Figure 1. Spectral and total down-welling solar flux at surface computed using SWNB2
975 for (a) standard clear-sky and cloudy-sky atmospheric profiles of mid-latitude winter
976 assuming solar zenith angle is 60° at the top of the atmosphere, and for (b) standard clear
977 sky profiles of mid-latitude and sub-Arctic winter with different incident solar zenith
978 angles.
979
980
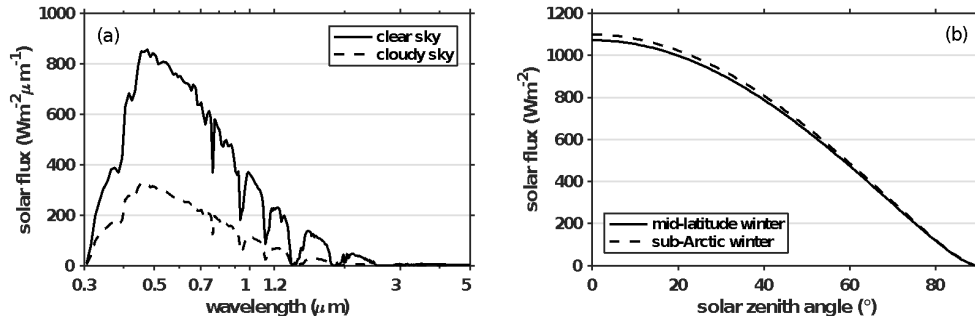
981
982
983

984 Figure 2. The spectral albedo of pure snow computed using 16-stream DISORT,
985 SNICAR, dEdd-AD, and 2SD models, for clear-sky (direct beam at solar zenith angle
986 60°) and cloudy-sky conditions in the left and right panels, respectively. The top panels
987 show spectral albedo. The middle panels show the difference ($\delta\alpha = \alpha_2 - \alpha_{16}$) in spectral
988 albedos computed using the two-stream model (α_2) and 16-stream DISORT (α_{16}). The
989 bottom panels show the difference of reflected spectral flux given $\delta\alpha$. The snowpack is
990 set to semi-infinite deep with grain radius of 100 μm.
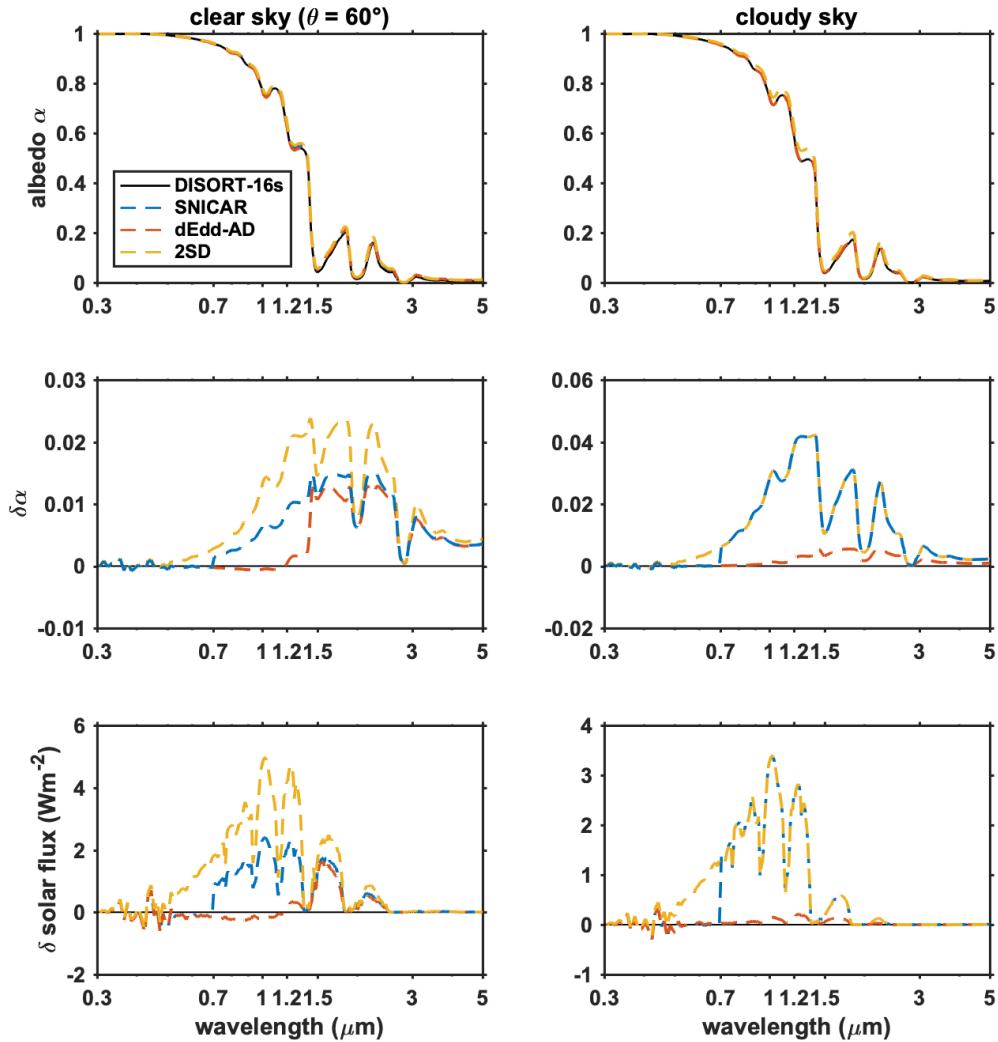
991
992
993

994 Figure 3. The difference in direct snow albedo ($\delta\alpha = \alpha_2 - \alpha_{16}$) computed using two-stream
995 models (α_2) and using 16-stream DISORT model (α_{16}), for various snow depths and solar
996 zenith angles, with snow grain radius of 100 μm. From the top to the bottom rows are
997 results of two-stream models SNICAR, dEdd-AD, and 2SD. From the left to the right
998 columns are albedo differences of all-wave, visible, near-IR bands.
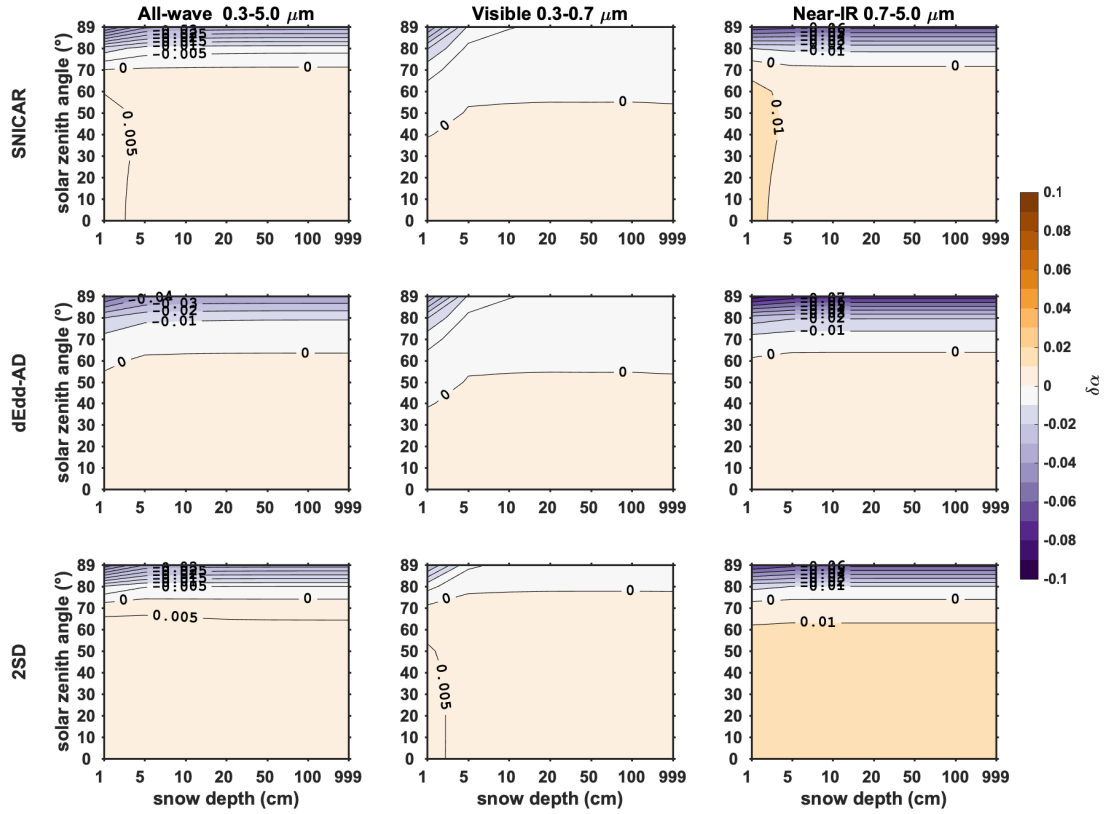
999
1000
1001

1002   Figure 4. The difference in direct snow albedo ($\delta\alpha = \alpha_2 - \alpha_{16}$) computed using two-stream
1003   models (α_2) and using 16-stream DISORT model (α_{16}), for various snow depths and solar
1004   zenith angles, with snow grain radius of 1000 μm.
1005
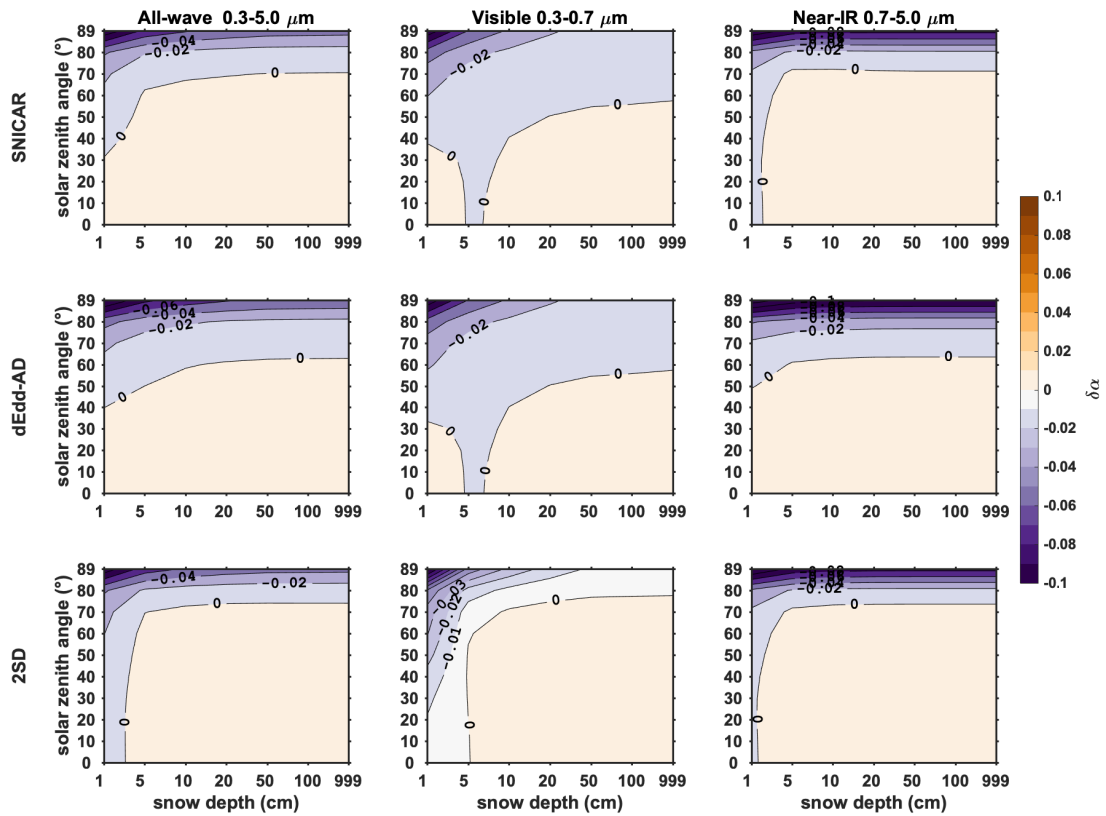
1006
1007
1008

1009   Figure 5. The difference in direct snow albedo ($\delta\alpha = \alpha_2 - \alpha_{16}$) computed using two-stream
1010   models (α_2) and using 16-stream DISORT model (α_{16}), for various snow depths and snow
1011   grain radii, with solar zenith angle of 60°.
1012
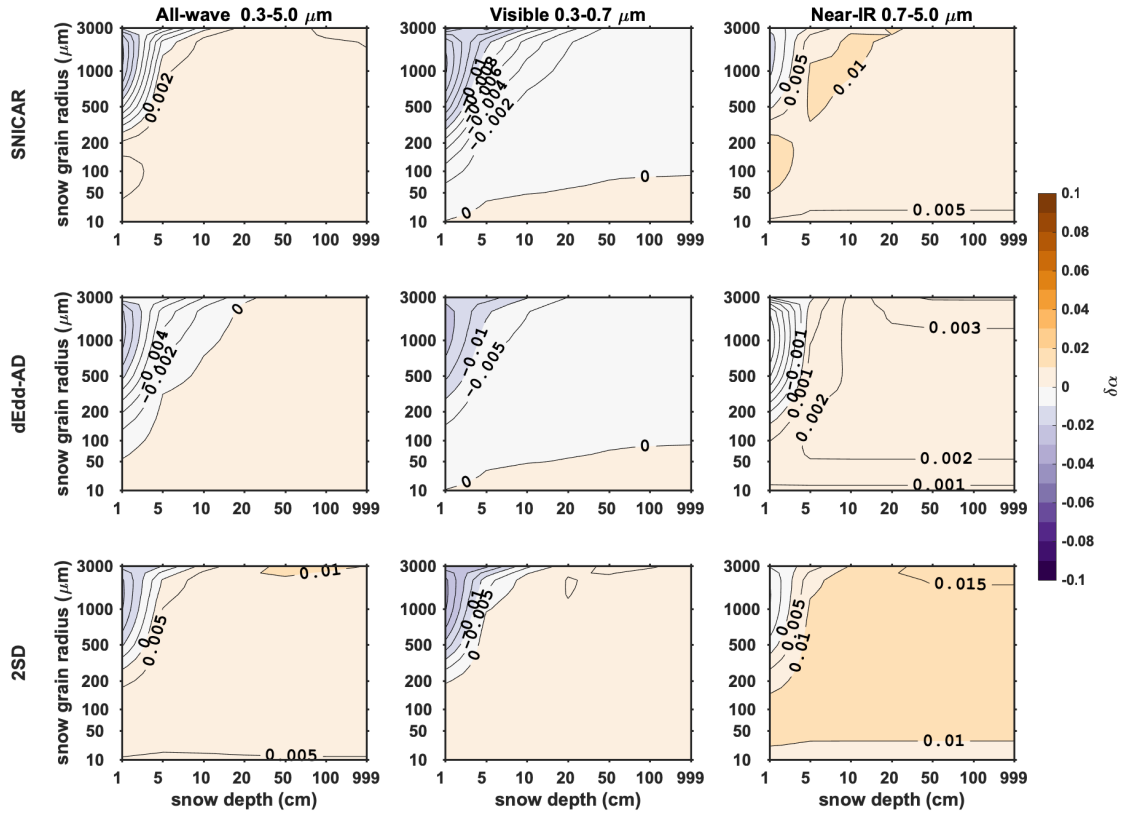
1013
1014

1015   Figure 6. The difference in diffuse snow albedo ($\delta\alpha = \alpha_2 - \alpha_{16}$) computed using two-
1016   stream models (α_2) and using 16-stream DISORT model (α_{16}), for various snow depths
1017   and snow grain radii, with solar zenith angle of 60° at the top of the atmosphere.
1018
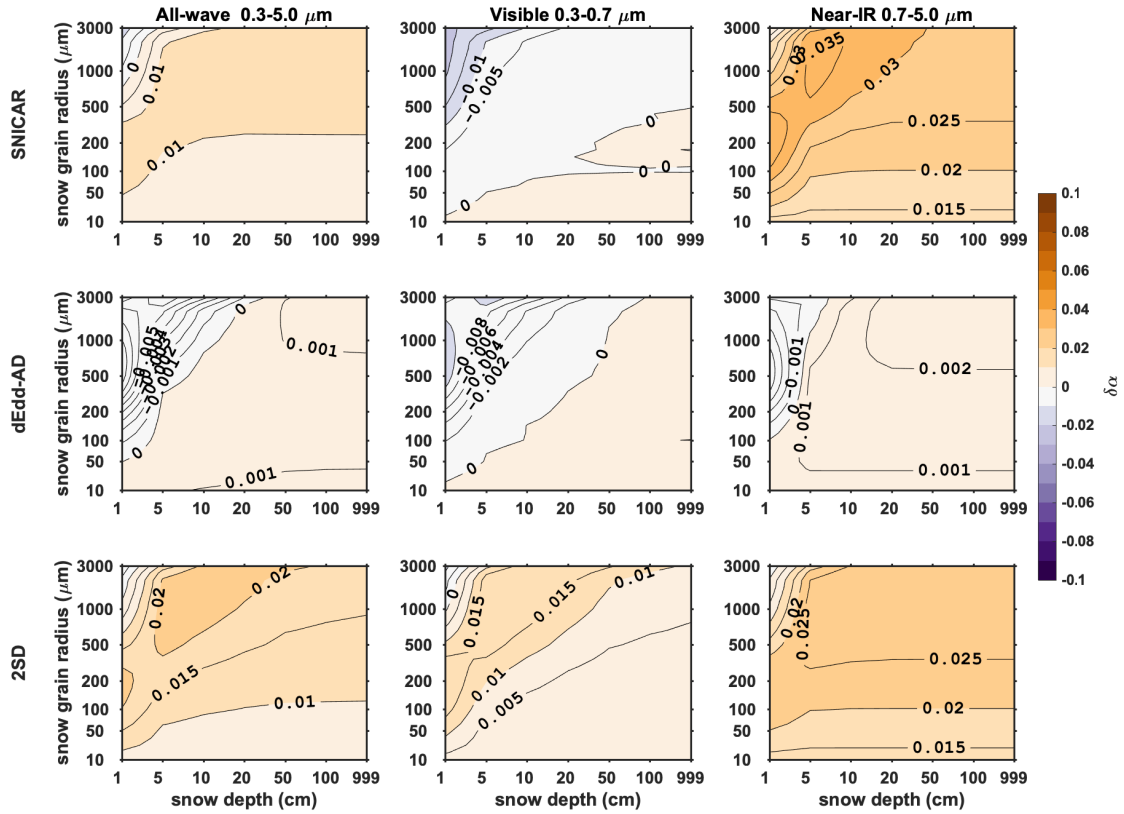
1019

1020   Figure 7. Error in reflected direct solar flux given albedo errors shown in Figure 3.
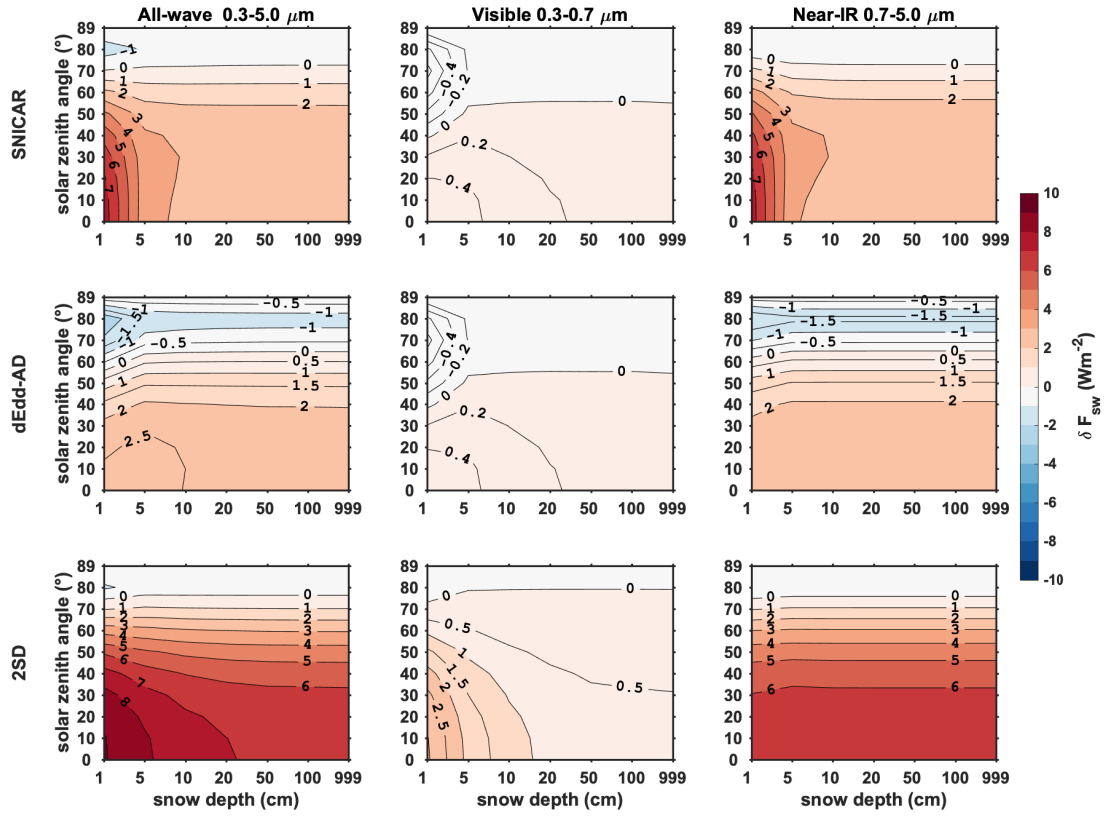
1021
1022

1023   Figure 8. Error in reflected direct solar flux given albedo errors shown in Figure 4.
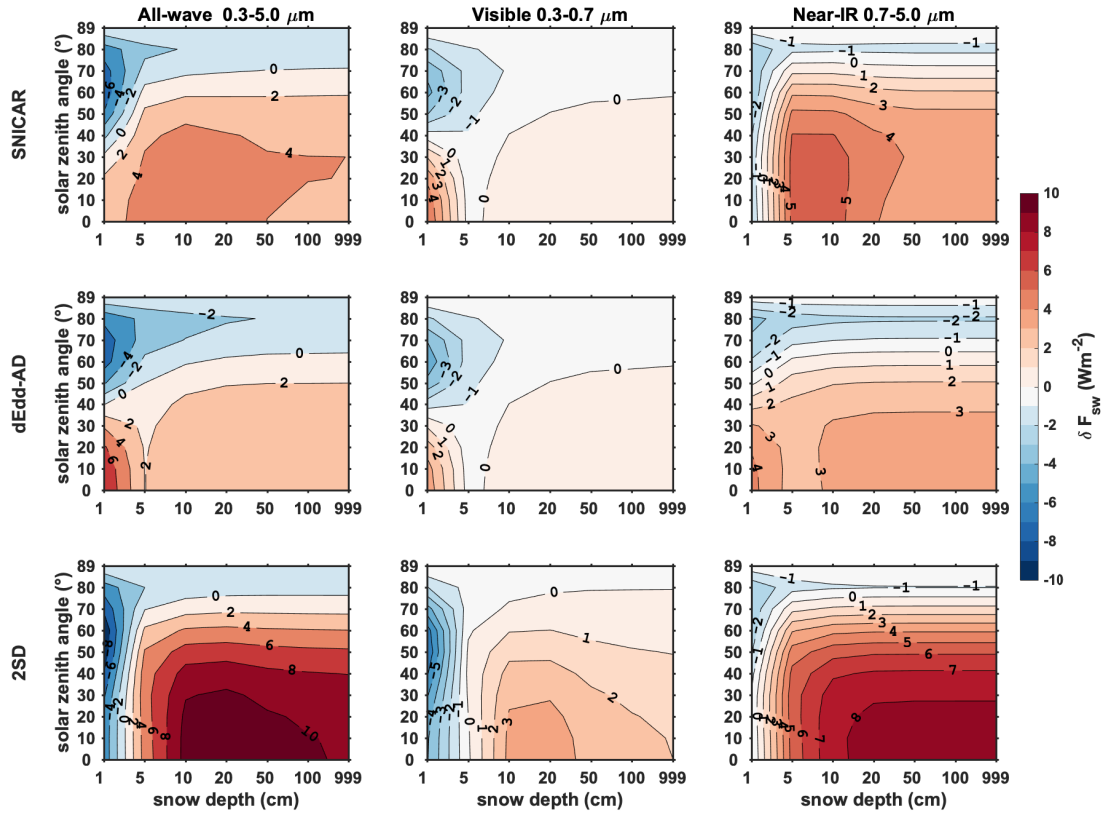
1024
1025
1026

1027   Figure 9. Error in reflected diffuse solar flux given albedo errors shown in Figure 6.
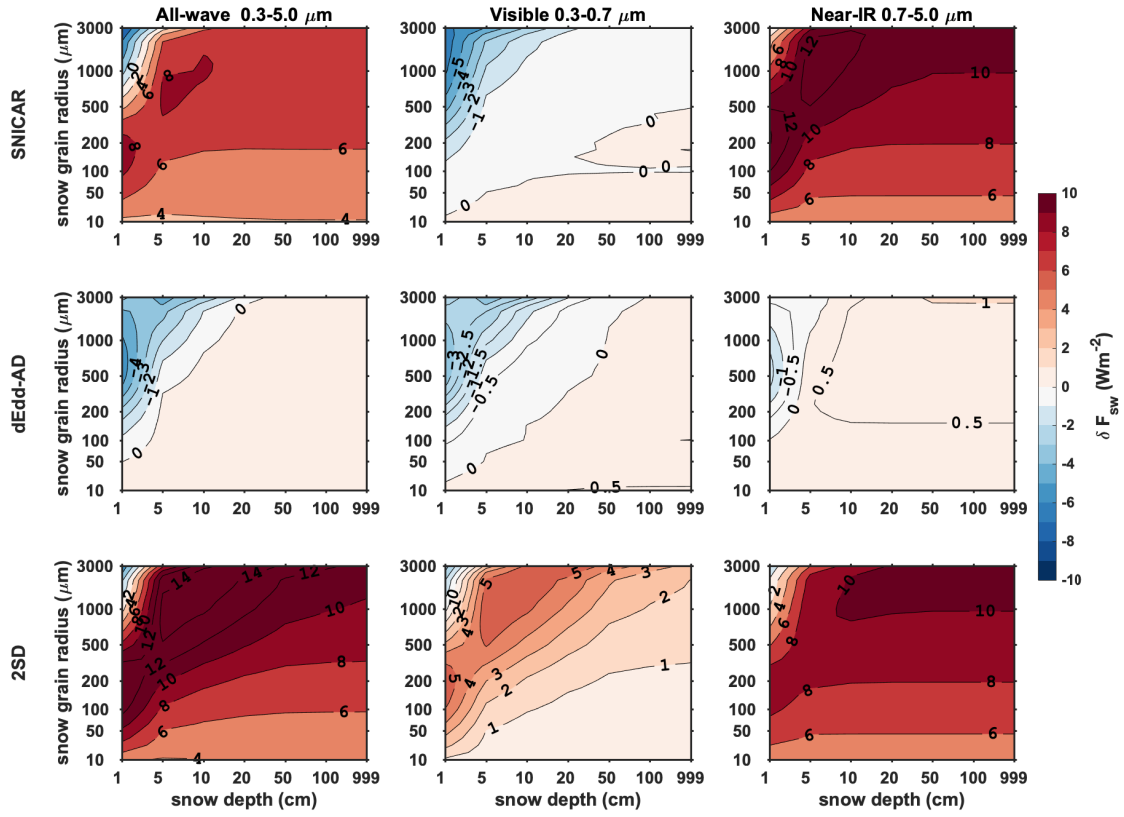
1028
1029
1030

1031 Figure 10. Comparison of light-absorption profiles derived from two-stream models and
1032 16-stream DISORT. The left-most column shows fractional band absorptions computed
1033 using 16-stream DISORT. The right three panels show the errors of all-wave, visible, and
1034 near-IR fractional absorptions calculated using two-stream models. The top and bottom
1035 panels are for clear-sky and cloudy-sky conditions (solar zenith angle of 60°),
1036 respectively. The snowpack is 10 cm deep and is divided evenly into five 2-cm thick
1037 layers, for new snow (r = 100 μm) and old snow (r = 1000 μm). The layers 1-4 represent
1038 the top four snow layers (top 8 cm), and layer 5 represents underlying ground with albedo
1039 of 0.25.
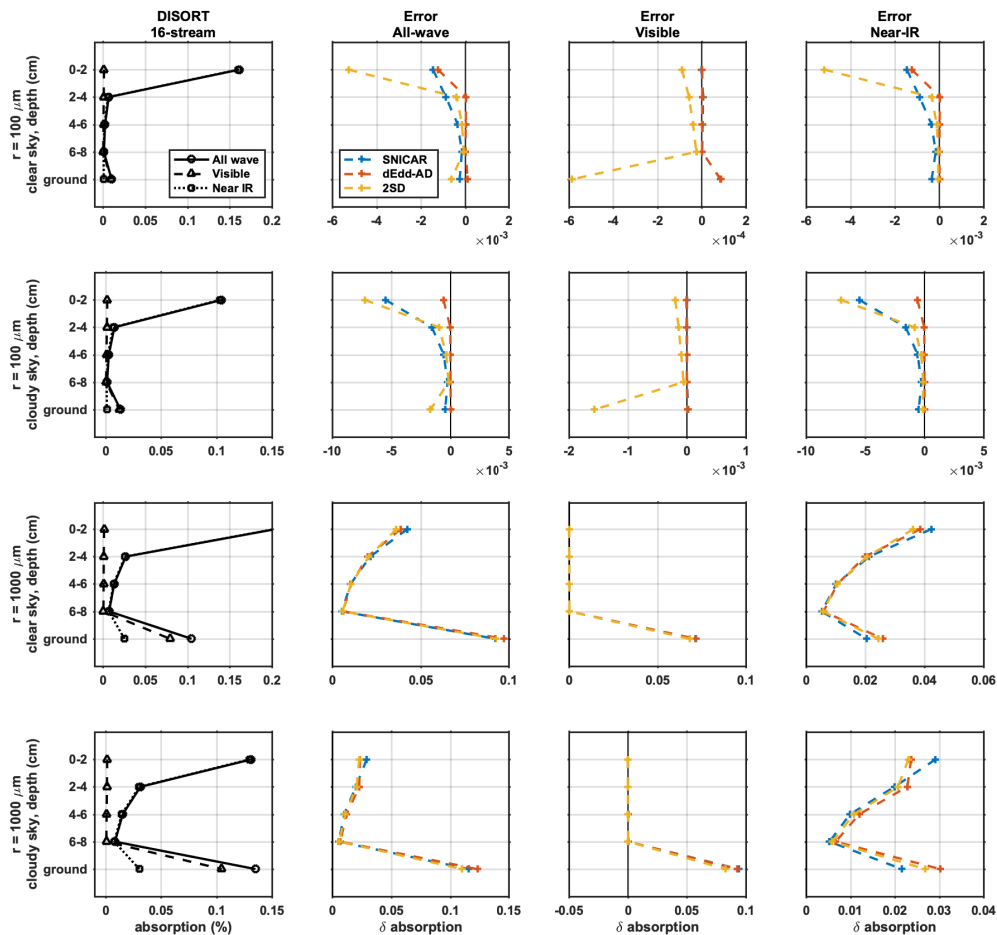
1040
1041

1043 Figure 11. (a) Direct near-IR snow albedo and (b) near-IR fractional absorption by top 2-
1044 cm snow of a 2-m thick snowpack, for solar zenith angles larger than 70° and snow grain
1045 radii of 100 μm and 1000 μm. (c) The ratios of near-IR albedo computed using CICE to
1046 that computed using 16-stream DISORT for different solar zenith angles. These ratios are
1047 parameterized as linear functions of the logarithmic of snow grain radius. The slopes and
1048 y-intercepts are shown in (d). The black dashed curves in figures (c) and (d) are fitting
1049 values computed using parameterization discussed in Section 5.
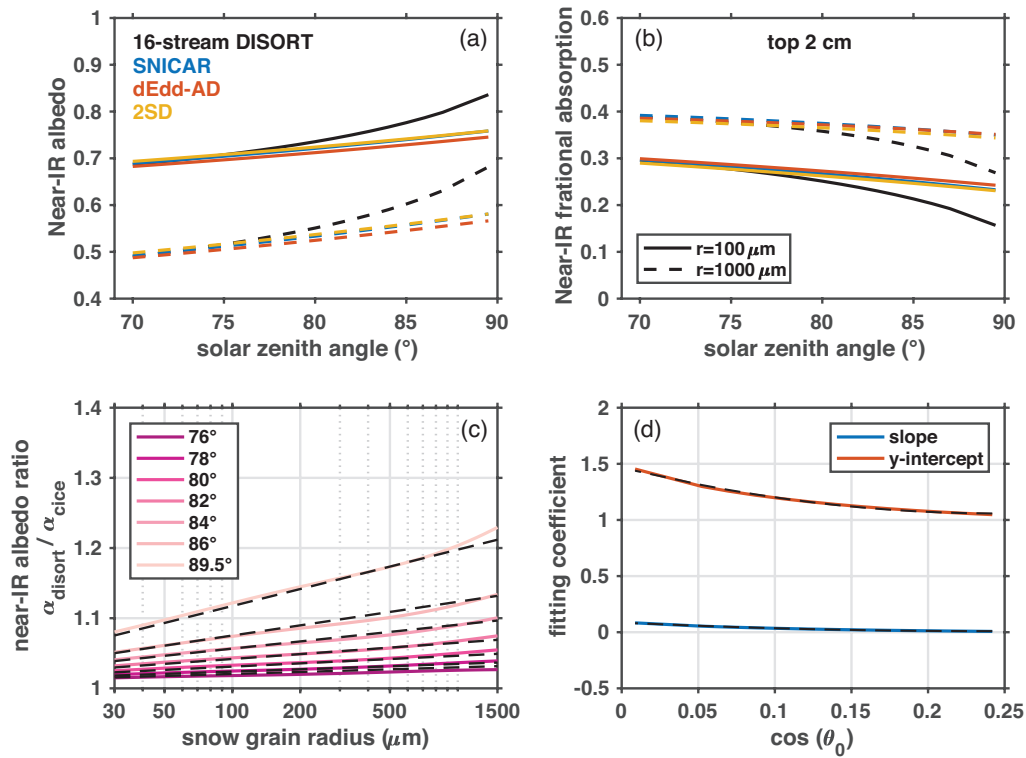
1050
1051
1052
1053

1054   Figure 12. Error in semi-infinite snow albedo computed using dEdd-AD before (top row)
1055   and after (bottom row) incorporating corrections for near-IR albedo, for different solar
1056   zenith angles and snow grain radii.
1057
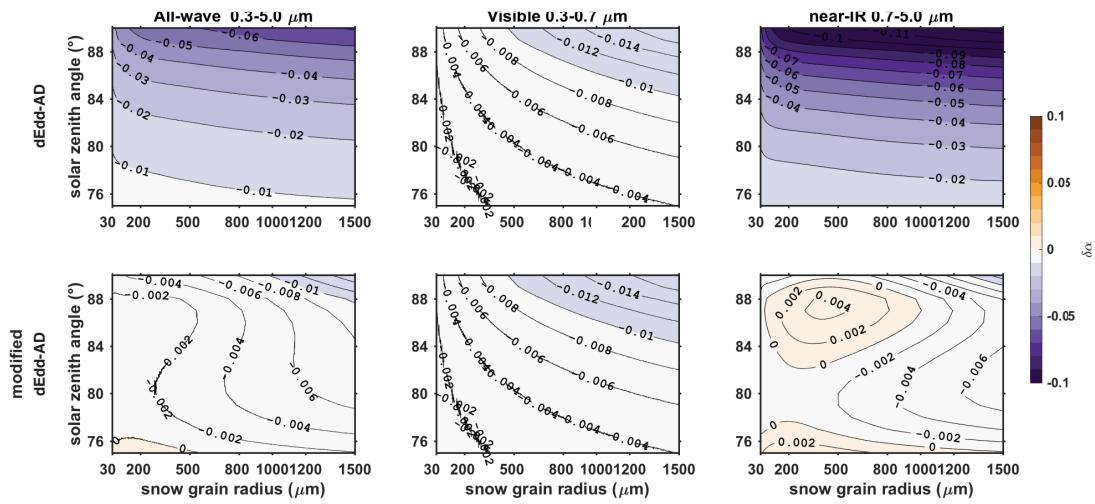
1062 Table 1. Acronyms used in this paper and their references.
1063
1064

ESM/ESMs	Earth System Models	
E3SM	Energy Exscale Earth System Model	Global climate model, previously know as ACME, https://e3sm.org/
CESM	Community Earth System Model	Global climate model, http://www.cesm.ucar.edu/
CCSM	Community Climate System Model	Global climate model, http://www.cesm.ucar.edu/models/ccsm4.0/
RACMO	Regional Atmospheric Climate Model	Regional climate model, https://www.projects.science.uu.nl/iceclimate/models/racmo.php
CAM	Community Atmospheric Model	Atmospheric model, Neale et al., 2012
ELM	E3SM land model	Land component of E3SM, https://e3sm.org/model/e3sm-model-description/v1-description/
CLM	Community land model	Land component of CESM, http://www.cesm.ucar.edu/models/clm/
MPAS-seaice	Model for Prediction Across Scales Sea Ice	Sea-ice component of E3SM, Turner et al., 2018
CICE	Los Almos Sea Ice Model	Sea-ice component of CESM, Hunke et al., 2010
RRTM	Rapid Radiative Transfer Model	Standalone column radiative transfer model, Mlawer and Clough, 1997, http://rtweb.aer.com/rrtm_frame.html
RRTMG	Rapid Radiative Transfer Model for GCM components	Modified RRTM for GCM application, Iacono et al., 2008, http://rtweb.aer.com/rrtm_frame.html
DISORT	DIScrete-Odinate Radiative Transfer model	Standalone column radiative transfer model, http://lllab.phy.stevens.edu/disort/, Stamnes et al., 1988
SWNB2	Shortwave Narrowband Model	Standalone column radiative transfer model, Zender et al., 1997; Zender, 1999
SNICAR	SNow ICe and Aerosol Radiative module	Snow module used in ELM and CLM, Flanner and Zender, 2005; Toon et al., 1989

dEdd-AD	Two-stream delta-Eddington Adding-Doubling radiative transfer algorithm	Sea-ice radiative transfer core in MPAS-seaice and CICE, Briegleb and Light, 2007
2SD	Two-Stream Discrete ordinate radiative transfer algorithm	Radiative transfer algorithm tested in this work, Jin and Stamnes, 1994
SNICAR-AD	SNICAR – Adding Doubling	Hybrid snow/sea-ice radiative transfer model, Section 8
SSP/SSPs	Single-Scattering Properties	Single-scattering albedo ϖ, asymmetry factor g, extinction coefficient σ_{ext}
near-IR	Near Infrared band	Wavelengths of 0.7 - 5 μm

1065
1066

1067
1068 Table 2. Two-stream radiative transfer algorithms evaluated in this work, including
1069 algorithms that are currently implemented in Earth System Model CESM and E3SM.
1070
1071

ESM Component	Land	Sea Ice	
Model	SNICAR	dEdd-AD	2SD
Radiative transfer approximation	two-stream δ-Eddington (visible) δ-Hemispheric-mean (near-IR)	two-stream δ-Eddington	two-stream δ-Discrete-ordinate
Treatment for multi-layered media	matrix inversion	adding-doubling	matrix inversion
Fresnel reflection/refraction	no	yes	yes
Number of bands implemented in ESMs	5 bands (1 visible, 4 near-IR)	3 bands (1 visible, 2 near-IR)	
Applies to	snow	bare/ponded/snow-covered sea ice, and snow	bare/ponded/snow-covered sea ice, and snow

1072